

QULABS SOFTWARE INDIA PVT. LTD.



PROJECT REPORT

**Quantum Memory & Quantum Frequency
Conversion with Rubidium Atoms at
Room Temperature**

Authors:

Ujjwal Gautam

Vedansh Nehra

Saket Priyam

Raj Abhinav

Contents

List of Figures	iv
1 Introduction to Quantum Memories	1
1.1 Introduciton to Quantum Memories	1
2 Theory	3
2.1 Saturation Absorption Spectroscopy (SAS)	3
2.2 3-Level Atomic system	7
2.2.1 Hamiltonian for Atom-Light Interaction	7
2.2.2 Master Equation	9
2.2.3 Field Propagation Equation	11
2.3 EIT with zero detuning of control	12
2.4 EIT with Off-Resonant Control Field	12
2.5 Slowing of Light	14
3 Basic Experiments	16
3.1 Spot Size Measurement	16
3.2 SAS	18
3.3 Laser Locking	19
3.4 Phase locking of probe and Control field	20
3.5 Observation of EIT Window	20
3.6 Pulse generation using AOM	23
3.6.1 AOM alignment	23
3.6.2 Frequency Shift	23
3.6.3 Delay, Rise, and Fall time of AOM	23
3.6.4 Amplitude Modulation	24

4 Quantum Memory	26
4.1 Laser Preparation	26
4.2 Pulse Synchronization	27
4.3 Qubit Encoding & Decoding	28
4.3.1 Polarization Encoding	28
4.3.2 Time-Bin Encoding	29
4.4 Storage & Retrieval	30
4.5 Detection	31
4.5.1 Semi-Classical Pulse	31
4.5.2 Single-Photon Pulse	31
5 Frequency Filtering	33
5.1 Etalons	34
5.2 Faraday Rotators	34
5.2.1 Faraday Isolator	34
5.3 Longpass Filter	37
5.4 Bandpass Filter	37
6 Introduction and Theory of Quantum Frequency Conversion	39
6.1 Introduction	39
6.2 Theory and Mathematical Model	40
6.3 Simulation	42
7 QFC	44
7.1 Laser Preparation	44
7.1.1 Laser Locking using CoSy	44
7.1.2 Laser Locking using Two-Photon Transition	44
7.2 Experimental Setup	44
8 Integrating What We Have Covered	45
8.1 Integrated Setup of Polarization Encoded Qubits	45
8.2 Integrated Setup of Time-bin Encoded Qubits	46

9 Miniaturisation of Concepts and Experiments	47
9.1 Gauss Chamber Design	47
9.1.1 Magnetic Shielding	47
9.1.2 Heating Unit	48
9.2 Gauss Chamber Design	49
9.3 Filtering Unit	50
9.3.1 Temperature Controlled Etalons	50
9.3.2 Faraday Rotator	50
9.4 Quantum Memory Unit	50
9.4.1 Polarization Encoding	50
9.4.2 Time Bin Encoding	50
Resolution of Time Bin Encoding	51
9.5 Quantum Frequency Conversion	51
9.5.1 Two-Photon Laser Locking Module	51
9.5.2 QFC Module	51
10 Instruments and Vendors	52
10.1 Laser System	52
10.2 Wavelength Meter	53
10.3 Beam Master for Beam profile measurement	54
10.4 Power Meter	54
10.5 Acousto Optic Modulator	55
10.6 Oscilloscope and Pulse generator	56
10.7 Photo Detectors	57
10.8 Rubidium Vapor Cell	57
10.9 Gauss Chamber	58
10.10 Fabry-Perot Interferometer	58

List of Figures

2.1	Blue lines depict Doppler-broadened transitions. Solid red and green lines depict the hyperfine transitions. Dashed red and green lines depict cross-over transitions. Red and green lines corresponds to transitions from the two ground states respectively. Note that the 4 blue lines are the four Doppler broadened peaks observed in the Doppler Spectrum of Rubidium. Also, observe the frequency splittings between the hyperfine lines. They are so small compared to the Doppler linewidth of the Rb atoms that they are not resolved in a Doppler broadened spectra. Therefore we use SAS (Doppler free spectroscopy) technique to resolve the hyperfine lines as shown in fig. 2.2	3
2.2	SAS Spectrum	4
2.3	Experimental setup for Saturated Absorption Spectroscopy. The reference and overlap (probe) beam are detected on a balanced photodetector.	5
2.4	Absorption of probe and pump beams by the ground-state atoms depends on the Doppler shift of the laser frequency ν to the transition frequency ν_1 by the atoms' thermal velocity: (a) $\nu < \nu_1$;(b) $\nu = \nu_1$ and (c) the crossover situation when $\nu_1 < \nu < \nu_2$ and the two transitions ν_1 and ν_2 are within a Doppler width of each other.	6
2.5	A three-level energy diagram showing probe (α, E_1, δ) and control (Ω, E_2, Δ) fields creating transitions between $g \leftrightarrow e$ and $s \leftrightarrow e$, respectively.	7
2.6	Use figure with detuning = 100 MHz(Top) Transmission vs detuning and Refractive index vs detuning of probe beam is plotted when the control is OFF (dashed, blue), control is ON and $\Delta = 0$ (dotted, gray), and control is ON and $\Delta \neq 0$ (solid, purple).	13

2.7 (a)The control field (red) optically pumps all of the atoms (green dots) into the ground state $ g\rangle$ Before the EIT medium, the signal pulse (blue) propagates with $v_g \approx c$. (b) The intensity of the control field remains constant. Upon entering the cell, the signal pulse experiences a reduced $v_g \ll c$, causing the signal pulse to spatially compress. An atomic spin wave is created along the cell in the direction of the pulse propagation, as illustrated by the rotated atomic spins. (c) When most of the signal pulse is inside the cell, the control field is extinguished, which sends $v_g = 0$, and maps any information encoded in the signal pulse onto the spin wave. (d) After a prescribed amount of time, the control field is turned on, releasing the spin wave into the signal field, which leaves the cell.	14
3.1 You can see the measurements for the semi-major and semi-minor axes of the spot size. You can also observe where the beam falls on the CBM's window and how far it is from the centre	16
3.2 This is how the heat profile (heat map) will be displayed on the software. This lets us know how uniformly the power is distributed in the beam.	17
3.3 Experimental setup of SAS performed in our lab. Notice that we have used only overlap beam for this purpose. DLC Pro controller is used to lock the laser at any peak in the spectrum observed on the oscilloscope.	18
3.4 Hyperfine spectrum of Rubidium collected from our experimental setup. The Fabry-Perot spectrum acts as a scale to measure the frequencies of the HF spectra. The separation of 6.8 GHz between the ground states is roughly verified by the plot.	19
3.5 HWP-Half Wave Plate, PBS - Polarizing Beam Splitter, GTP - Glan Taylor Polarizer, PD - Photodetector, CoSy - Compact Spectroscopy . .	20
3.6 EIT window as observed in the DLC Pro module (left) and on the Oscilloscope (right) (yellow) with the smoothed curve (in purple) and the FPI output (green).The EIT windows have been circled.	22

3.7	Data from the oscilloscope as plotted in MATLAB. The FWHM has been calculated to be 6.643 MHz, which is in agreement with previously published papers and theoretical predictions.	22
3.8	Experimentally measured rise time (top left) and fall time (top right) of an AOM, and delay (bottom) between the input(purple) amplitude modulated signal and the AOM output(blue).	24
3.9	Left figure - Yellow is the input waveform for amplitude modulation. Green is the amplitude modulated output from the RF driver. Right figure - Gray is the amplitude modulated signal form the RF driver. Purple is the corresponding AOM output, with a delay and distortion due to the limitation of the rise and the fall time of the AOM.	25
4.1	Input Preparation for Probe and Control Pulses	26
4.2	Polarization Encoding Using a HWP	28
4.3	Unbalanced MZI with Prism	29
4.4	Timing Diagram of Control and Probe Pulses (The time scale is in ns.) .	30
4.5	Principle of the TCSPC technique [13]	32
5.1	Frequency Filtering Setups	33
5.2	Transmission profiles (w.r.t wavelength) from the two etalons (Left). Overall transmission from the series combination of the two etalons (Right)	35
5.3	Diagram depicting overall working of the Faraday Rotator. FI stands for Faraday Isolator	36
5.4	37
5.5	Working of an optical bandpass filter. CWL stands for Central Wavelength	38
6.1	Diamond atomic scheme use for frequency conversion	40
6.2	Density Matrix for 4-level transition	42
6.3	Intensity-Time curve obtained from the simulation of the frequency conversion process	43

8.1	Experimental Setup Integrating QM, Frequency Filtering and QFC using Polarization Encoded Qubits	45
8.2	Experimental Setup Integrating QM, Frequency Filtering and QFC using Time Bin Encoded Qubits	46
9.1	Full Diagram of Gauss Chamber	48
9.2	Inside view of Gauss Chamber	48
9.3	Increasing the time difference between $ early\rangle$ and $ late\rangle$	51
10.1	Schematic internal components of an ECDL Laser. Source: [37]	52
10.2	Schematic of a Wavelength Meter. Source: HighFinesse Datasheet	53
10.3	Software interface of Coherent Beam Master. It measures the beam diameter along V and W axis. It also gives the heatmap of the intensity of the laser beam. Source: Coherent Beam Master Datasheet.	54
10.4	Powermeter with a sensing unit and a screen to display the power falling on it upto 100 nW level. Source: CNI Optics Inc.	55
10.5	Schematic of an AOM aligned in the +1 order. An AOM from IntraAction is shown on the right. Source: IntraAction.	56
10.6	Oscilloscope from Keysight Technologies used for generating pulses and displaying signals. Source: Keysight Technologies.	56
10.7	Silicon gain adjustable photodetector from Thorlabs Inc. Source: Thorlabs.	57
10.8	Borosilicate Rb vapor cell from Thorlabs Inc. Source: Thorlabs.	58
10.9	A typical design of a Gauss Chamber. It has three-layers of μ -metal shielding in a cylindrical box with holes of size of the diameter of the Rb vapor cell on the end-caps.	58
10.10	Fabry-Perot interferometer used in our lab with its typical spectrum beside it. The separation of the peaks is a characteristic of the FPI. We use an FPI with FSR = 1GHz. Source: Toptica Photonics.	59

Chapter 1

Introduction to Quantum Memories

1.1 Introduciton to Quantum Memories

Quantum information processing is the most emergent technology widely used in long-distance quantum communication, quantum key distribution (QKD)[35], and quantum internet[24]. Quantum technologies are used in sophisticated and ultra-precision measurement such as metrology [17],[16] and quantum magnetometry [5]. Quantum computing offers the solution to a particular computationally hard problem that cannot be solved using classical computation methods. Several extraordinary properties make it very powerful in quantum technology, for instance, quantum entanglement, quantum teleportation, no-cloning theorem, etc. Most significant advances have been made in quantum cryptography in the form of QKD. Quantum memory (QM)[26, 36, 20, 8, 18] is the central part of all the devices that are used in Quantum technology, for instance, the quantum repeaters[7], quantum routers [2] used in QKD and Quantum Internet as the essential component. The work of QM is to store the quantum information data in the form of qubit strings for a significant amount of time and retrieve it when called for demand [21, 25]. It is also crucial for synchronizing all the demand and delivery of qubits in the channels of quantum networks. Quantum information data is so delicate that it can easily be decohere or get contemplated with noise when retrieved. Several error-correcting techniques can be used to correct systematic error up to the threshold [12][9].

In the development of quantum memory, engineered couplings to multiple degrees of freedom such as electronic, magnetic, vibrational, and hybrid are actively explored in trapped, warm, cold, or Bose-condensed atoms, in crystalline and amorphous solids, molecular gases, structured media, and meta-materials. Based on their used techniques, physical systems, and involved mechanisms, quantum memory can be classified in various ways— Based on the requirement of temperature, it can be categorized in room temperature QM[22][34] and low cryogenic temperature QM[1]. Both have multiple technological challenges; for instance, QMs at cryogenic temperature offer less decoherence and can easily decouple with the environment but are expensive and not very pragmatic for quantum network and internet expectations. Based on techniques used, for instance, quantum control, QMs are categorized as optical controlled quantum memory like EIT, ATS based, and off-resonant Raman memory and engineered absorption quantum memory like AFC based and echo-based QMs, i.e., CRIB/GEM.

Based on the control pulse mechanism, quantum memories can be categorized broadly into two categories. The first one is called the adiabatic memory, in which slowly varying control pulse is applicable. Some of the popular protocols under adiabatic memory are EIT and Off resonant Raman memory protocols. These memories use the elimination of absorption as their mechanism because of their adiabatic nature. These memories are slow but are highly efficient. The second category is called fast memory, the control pulse involved here in the form of π -pulses. Some of the popular protocols which come under it are CRIB, GEM, and AFC. The difference between them is that fast memories use absorption instead of eliminating it. These memories are broadband-focused and fast, with the retrieval at a predetermined time. The choice of a variety of media used for the fast memories is also more significant than their adiabatic counterparts [18][26].

Currently, our work focuses specifically on atomic ensemble-based implementations. We discuss the theory behind the EIT-based QM and then propose experiments to demonstrate the POC of the QM. We also list out the instruments used in the experiments and the vendors supplying them. Then we present a compact model of QM and its components.

Chapter 2

Theory

2.1 Saturation Absorption Spectroscopy (SAS)

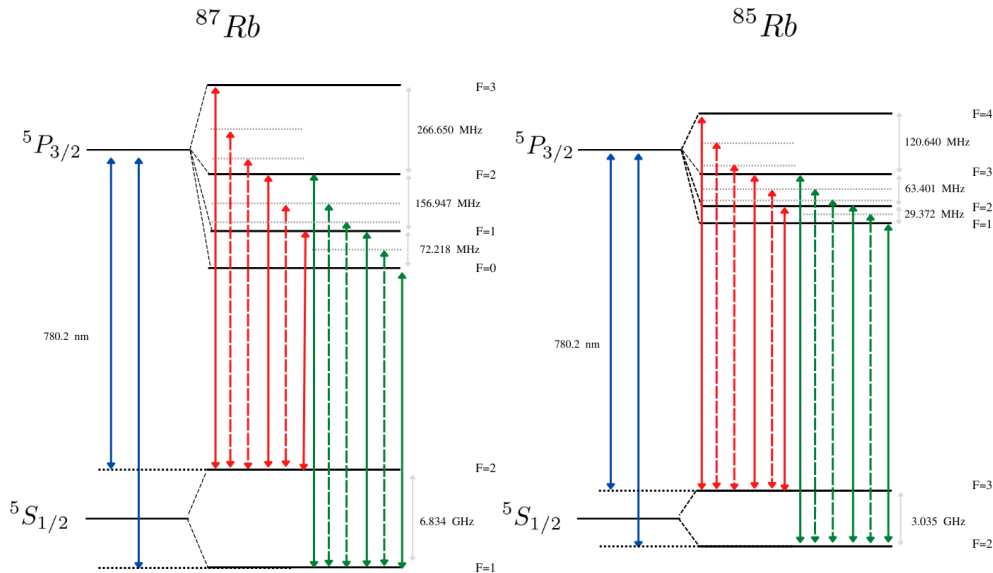


FIGURE 2.1: Blue lines depict Doppler-broadened transitions. Solid red and green lines depict the hyperfine transitions. Dashed red and green lines depict cross-over transitions. Red and green lines corresponds to transitions from the two ground states respectively. Note that the 4 blue lines are the four Doppler broadened peaks observed in the Doppler Spectrum of Rubidium. Also, observe the frequency splittings between the hyperfine lines. They are so small compared to the Doppler linewidth of the Rb atoms that they are not resolved in a Doppler broadened spectra. Therefore we use SAS (Doppler free spectroscopy) technique to resolve the hyperfine lines as shown in fig. 2.2

The closely spaced lines are not resolved because of Doppler Broadening. The atoms due to thermal motion have a thermal distribution of velocities (Maxwell

distribution) and atoms at a different velocity receive Doppler shifted frequency. Hence, atoms with zero velocity in the direction of the laser will receive an unshifted frequency of light (ν_{laser}). Now, atoms with a velocity v_z will receive a shifted frequency of light given by $\nu_{laser} = \nu_{atom}(1 + v_z/c)$, where ν_{laser} is the frequency of laser source and ν_{atom} is the frequency received by the atom. We can also write $v_z = c(\nu_{laser} - \nu_{atom})/\nu_{atom}$, which means that atoms with velocity v_z will be resonant to the atomic transition ($\nu_{atom} = \nu_{resonant}$) when the laser is at frequency ν_{laser} . When $v_z > 0$, the atoms are moving in the direction of the laser beam; when $v_z < 0$ they are moving opposite to the laser. As the frequency of the laser is varied, the

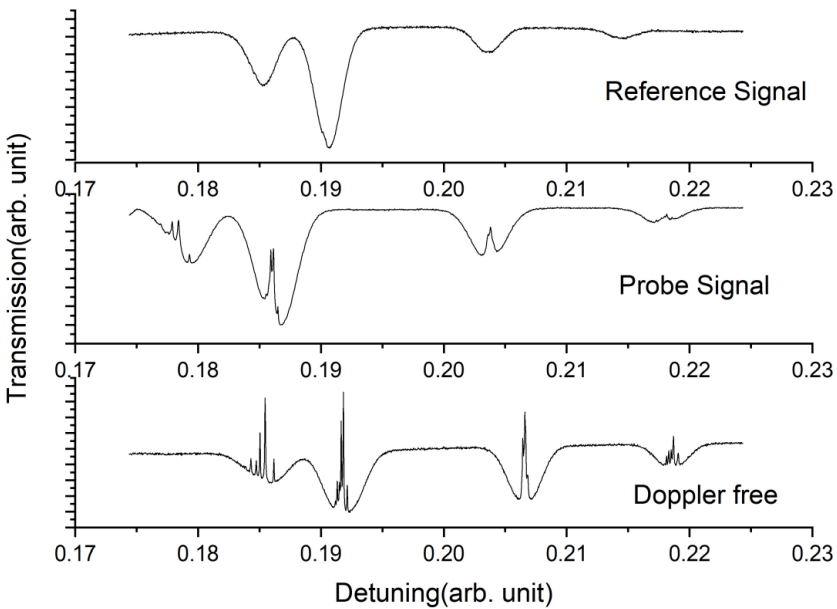


FIGURE 2.2: SAS Spectrum

light interacts with different parts of the thermal distribution of the velocities of the atoms.

Throughout the experiment, we focus mainly on the ^{87}Rb spectrum. Saturation Absorption Spectroscopy is a technique to help us understand the Hyperfine spectrum. The figure 2.3 (reproduced from [32]) shows the setup of SAS experiment. The diagram 2.3 shows that we divide the incoming laser beam into three beams known as reference, overlapping, and pump beams. The pump beam has a very high intensity compared to the other beams and is a saturating beam. Intense beams are saturating because they excite the atoms interacting with them and create a population inversion which is saturated, i.e. the population of excited atoms can no longer

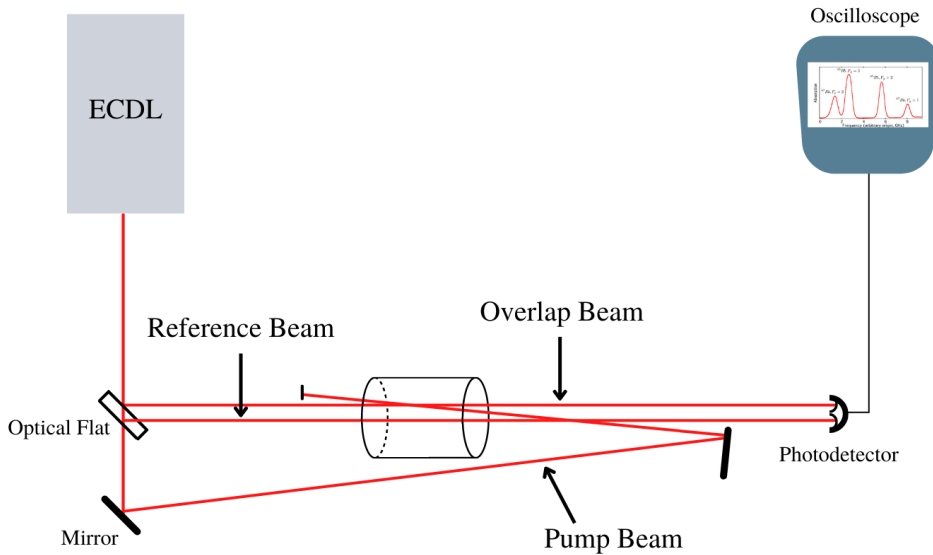


FIGURE 2.3: Experimental setup for Saturated Absorption Spectroscopy. The reference and overlap (probe) beam are detected on a balanced photodetector.

be increased. A weak probe beam thus can not further excite any atom, hence is not absorbed by the medium. We detect the reference beam and the overlapping beam (weak probe beams) on a balanced photodetector.

In this technique, two counterpropagating, overlapping laser beams of exactly the same frequency interact with atoms in a vapor. When the laser frequency is different from the resonant frequency of the atoms, ν_{resonant} , one beam interacts with a set of atoms with some velocity v_z and the other beam interacts with an entirely different set of atoms, those with velocity $-v_z$. However, when the frequency is tuned to ν_{resonant} , the two beams interact with the same group of atoms, those with velocity component parallel to the beams $v_z \approx 0$. Under these circumstances the stronger beam, the pump beam, reduces the absorption experienced by the weaker overlap probe beam but only over a very narrow range of frequencies that under proper conditions can approach the natural width determined by the lifetime of the atomic transition.

Figure 2.4 (a) and (b) occurs when we consider a single excited state. Now let us consider the case when there are two transitions sharing a common ground state and differ in frequency by less than the Doppler linewidth. In this situation there

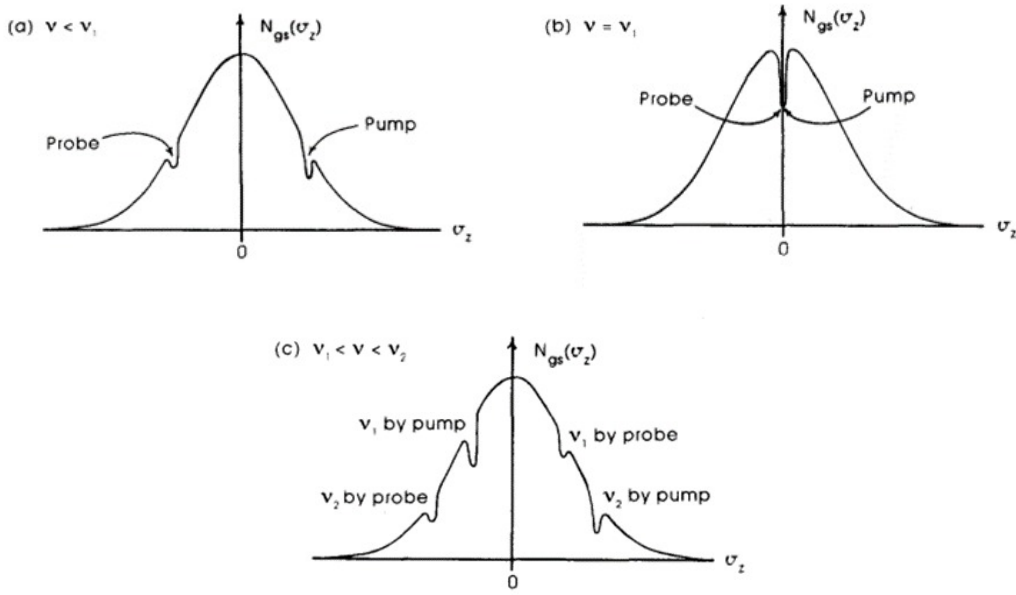


FIGURE 2.4: Absorption of probe and pump beams by the ground-state atoms depends on the Doppler shift of the laser frequency ν to the transition frequency ν_1 by the atoms' thermal velocity: (a) $\nu < \nu_1$; (b) $\nu = \nu_1$ and (c) the crossover situation when $\nu_1 < \nu < \nu_2$ and the two transitions ν_1 and ν_2 are within a Doppler width of each other.

are laser frequencies at which the pump beam interacts with two different groups of atoms at the same time. An example is shown in (c), where $\nu_1 < \nu_{laser} < \nu_2$ so that the atoms with velocity $-v_{z1}$ see ν_{laser} redshifted to ν_1 , while at the same time those with velocity $+v_{z2}$ see ν_{laser} blueshifted to ν_2 . The probe beam interacts in a similar way with atoms at $+v_{z1}$ and $-v_{z2}$. As the laser frequency is increased, the notches corresponding to the pump beam move left, and those of the probe beam move right. Clearly, there will be some laser frequency ν_c such that the same group of atoms will be resonant at ν_1 with the pump and at ν_2 with the probe (and another group at ν_1 with the probe and ν_2 with the pump). In both cases the pump beam reduces the population in the $F = 2$ level, and there is increased transmission of the overlapping probe beam giving rise to the extra dips, b, d, and e in Fig. 2.2 known as Crossover dips and correspond to crossover transition. Crossover frequency ν_c is $\nu_c = (\nu_1 + \nu_2)/2$ i.e. mid-frequency of any two atomic transitions.

2.2 3-Level Atomic system

This section has been taken from N.B. Phillips' PhD Thesis [31].

2.2.1 Hamiltonian for Atom-Light Interaction

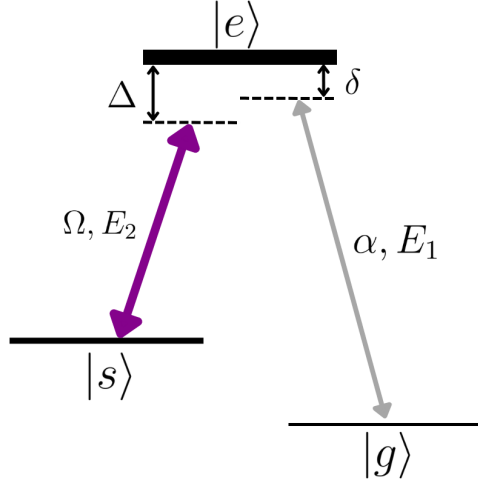


FIGURE 2.5: A three-level energy diagram showing probe (α, E_1, δ) and control (Ω, E_2, Δ) fields creating transitions between $g \leftrightarrow e$ and $s \leftrightarrow e$, respectively.

Hamiltonian of a atom-light interacting system is a sum of the atomic Hamiltonian, the electric fields Hamiltonian, and the interaction term between them. Here, we consider a semi-classical treatment of the fields and assume that the energy in the fields remain almost constant throughout the lifetime of the interaction. Therefore, we can safely drop the field Hamiltonian term[31].

$$H = H_a + H_f + H_i = H_a + H_i \quad (2.1)$$

where, H_a is the atomic Hamiltonian in the absence of external field,

$$H_a = 0|g\rangle\langle g| + \hbar\omega_{sg}|s\rangle\langle s| + \hbar\omega_{eg}|e\rangle\langle e| \quad (2.2)$$

and H_i is the Hamiltonian corresponding to the atom-light interaction,

$$H_i = -\hat{d} \cdot \mathbf{E}(z, t) \quad (2.3)$$

where, \hat{d} is the dipole operator of the atoms, and $\mathbf{E}(z, t)$ is the total external electric field. The dipole operator can be expanded in terms of $\hat{\sigma}_{ij}$ (Pauli Matrices) and dipole moments:

$$\begin{aligned}\hat{d} &= |e\rangle\langle e|\hat{d}|g\rangle\langle g| + |e\rangle\langle e|\hat{d}|s\rangle\langle s| + \text{H.c.} \\ &= \wp_{eg}\hat{\sigma}_{eg} + \wp_{es}\hat{\sigma}_{es} + \text{H.c.},\end{aligned}\quad (2.4)$$

The net electric field is the sum of the probe and the control electric field and is written in the semi-classical picture as:

$$\begin{aligned}\mathbf{E}(z, t) &= \hat{\varepsilon}_1\mathcal{E}_1(z, t)e^{ik_1z-iv_1t} + \hat{\varepsilon}_2\mathcal{E}_2(z, t)e^{ik_2z-iv_2t} + \text{c.c.} \\ &= \mathbf{E}^{(+)}(z, t) + \mathbf{E}^{(-)}(z, t)\end{aligned}\quad (2.5)$$

Where $\hat{\varepsilon}_{1/2}$ is the direction of polarisation of the field in spherical unit vector and $\mathcal{E}_{1/2}$ is the amplitude of the probe (1) and the control field (2). The positive and negative rotating part of the field are represented by the \pm superscript on E . The equation 2.3 can be written as:

$$\hat{H}_i = \langle e | \mathbf{d} \cdot \hat{\varepsilon}_1 | g \rangle \mathcal{E}_1(z, t) \hat{\sigma}_{eg} e^{ik_1 z - iv_1 t} + \langle e | \mathbf{d} \cdot \hat{\varepsilon}_2 | s \rangle \mathcal{E}_2(z, t) \hat{\sigma}_{es} e^{ik_2 z - iv_2 t} + \text{H.c.} \quad (2.6)$$

Putting H_i from equation 2.6 and H_a from equation 2.2 in H from equation 2.1, we get:

$$\frac{\hat{H}}{\hbar} = \omega_{sg}\hat{\sigma}_{ss} + \omega_{eg}\hat{\sigma}_{ee} - \left(\Omega\hat{\sigma}_{es}e^{ik_2 z - iv_2 t} + \alpha\hat{\sigma}_{eg}e^{ik_1 z - iv_1 t} + \text{H.c.} \right) \quad (2.7)$$

where, α and Ω are the Rabi frequencies of the probe and the control field respectively and are given by:

$$\begin{aligned}\Omega &= \langle e | \mathbf{d} \cdot \hat{\varepsilon}_2 | s \rangle \mathcal{E}_2 / \hbar \\ \alpha &= \langle e | \mathbf{d} \cdot \hat{\varepsilon}_1 | g \rangle \mathcal{E}_1 / \hbar\end{aligned}\quad (2.8)$$

The total Hamiltonian 2.7 can be written in its matrix form as:

$$\frac{\hat{H}}{\hbar} = \begin{bmatrix} 0 & 0 & \alpha e^{ik_1 z - iv_1 t} \\ 0 & \omega_{sg} & \Omega e^{ik_2 z - iv_2 t} \\ \alpha^* e^{-ik_1 z + iv_1 t} & \Omega^* e^{-ik_2 z + iv_2 t} & \omega_{eg} \end{bmatrix} \quad (2.9)$$

The Hamiltonian has time dependence in the phase term. We can remove the time dependence by shifting our basis to a rotating frame. Let us define the unitary transformation by $U(t)$, given by:

$$\hat{U}(t) = \begin{bmatrix} 1 & 0 & 0 \\ 0 & e^{-i(\nu_1 - \nu_2)t} & 0 \\ 0 & 0 & e^{-i\nu_1 t} \end{bmatrix} \quad (2.10)$$

The Hamiltonian is transformed by the equation:

$$\hat{H}_{new} = i\hbar \frac{\hat{U}^\dagger(t)}{t} \hat{U}(t) + \hat{U}^\dagger(t) \hat{H}(t) \hat{U}(t) \quad (2.11)$$

Substituting equations 2.9, 2.10, in 2.11 and ignoring the fast oscillating terms (Rotating Wave Approximation), the new Hamiltonian becomes,

$$\frac{\hat{H}_{new}}{\hbar} = - \begin{bmatrix} 0 & 0 & \alpha \\ 0 & \delta & \Omega \\ \alpha^* & \Omega^* & (\Delta + \delta) \end{bmatrix} \quad (2.12)$$

The quantities Δ and δ are the field detunings as shown in the energy level diagram and are equal to

$$\begin{aligned} \delta &= \nu_1 - \omega_{eg} \\ \Delta &= \nu_2 - \omega_{es} \end{aligned} \quad (2.13)$$

2.2.2 Master Equation

We evolve our atom-field system using the Liouville-von Neumann equation also known as the master equation, given by:

$$\begin{aligned} \frac{\partial \tilde{\rho}}{\partial t} &= \frac{1}{i\hbar} [\hat{H}_{new}, \tilde{\rho}] + \frac{\Gamma_{e \rightarrow g}}{2} [2\hat{\sigma}_{ge}\tilde{\rho}\hat{\sigma}_{eg} - \{\hat{\sigma}_{ee}, \tilde{\rho}\}] + \frac{\Gamma_{e \rightarrow s}}{2} [2\hat{\sigma}_{se}\tilde{\rho}\hat{\sigma}_{es} - \{\hat{\sigma}_{ss}, \tilde{\rho}\}] \\ &\quad + \frac{\gamma_{s,\text{deph}}}{2} [2\hat{\sigma}_{ss}\tilde{\rho}\hat{\sigma}_{ss} - \{\hat{\sigma}_{ss}, \tilde{\rho}\}] + \frac{\gamma_{e,\text{deph}}}{2} [2\hat{\sigma}_{ee}\tilde{\rho}\hat{\sigma}_{ee} - \{\hat{\sigma}_{ss}, \tilde{\rho}\}] \end{aligned} \quad (2.14)$$

where, $\tilde{\rho}$ is the atomic density matrix in the transformed basis. The second and third terms on the right-hand side describe spontaneous emission from states $|e\rangle$ to $|g\rangle$ and states $|e\rangle$ to $|s\rangle$ at rates $\Gamma_{e \rightarrow g}$ and $\Gamma_{e \rightarrow s}$, respectively, such that $\Gamma_e \equiv \Gamma_{e \rightarrow g} + \Gamma_{e \rightarrow s}$ is the total spontaneous emission rate out of $|e\rangle$, and thus $1/\Gamma_e$ is its

lifetime. Additionally, we have phenomenologically introduced energy conserving dephasing processes (e.g. collisions with inert atomic species) with rates $\gamma_{s, \text{deph}}$ and $\gamma_{e, \text{deph}}$. We further define the coherence decay rates as

$$\gamma_{eg} = \frac{1}{2} (\Gamma_e + \gamma_{e, \text{deph}}) \equiv \gamma \quad (2.15)$$

$$\gamma_{sg} = \frac{1}{2} \gamma_{s, \text{deph}} \equiv \gamma_0 \quad (2.16)$$

$$\gamma_{es} = \frac{1}{2} (\Gamma_e + \gamma_{s, \text{deph}} + \gamma_{e, \text{deph}}) \quad (2.17)$$

It is notable that in the limit of radiative decoherence ($\gamma_{i, \text{deph}} = 0$), γ_{ej} will be equal to half of the spontaneous decay rate out of $|e\rangle$. The density matrix equations of motion are:

$$\partial_t \tilde{\rho}_{gg} = \Gamma_{31} \tilde{\rho}_{ee} - i\alpha \tilde{\rho}_{ge} + i\alpha^* \tilde{\rho}_{eg} \quad (2.18)$$

$$\partial_t \tilde{\rho}_{ss} = \Gamma_{32} \tilde{\rho}_{ee} - i\Omega \tilde{\rho}_{se} + i\Omega^* \tilde{\rho}_{es} \quad (2.19)$$

$$\partial_t \tilde{\rho}_{eg} = -[\gamma - i(\Delta + \delta)] \tilde{\rho}_{eg} + i\Omega \tilde{\rho}_{sg} + i\alpha (\tilde{\rho}_{gg} - \tilde{\rho}_{ee}) \quad (2.20)$$

$$\partial_t \tilde{\rho}_{es} = -(\gamma_{es} - i\Delta) \tilde{\rho}_{es} + i\alpha \tilde{\rho}_{gs} + i\Omega (\tilde{\rho}_{ss} - \tilde{\rho}_{ee}) \quad (2.21)$$

$$\partial_t \tilde{\rho}_{sg} = -(\gamma_0 - i\delta) \tilde{\rho}_{sg} + i\Omega^* \tilde{\rho}_{eg} - i\alpha \tilde{\rho}_{se} \quad (2.22)$$

We solve the system of ODEs by taking some assumptions:

- Probe field is weaker than the control field. $\alpha \ll \Omega$
- Therefore, the population transfer is very small. Thus we can put, $\rho_{gg} \approx 1$ and $\rho_{ss} = \rho_{ee} \approx 0$.
- Also, $\rho_{es} = 0$.
- We consider steady-state condition. So we can write, $\partial_t \tilde{\rho} = 0$.

We solve these equations numerically and plot the absorption curve ($Im(\rho_{eg})$) and the refractive index curve ($Re(\rho_{eg})$) versus the probe detuning (δ) in fig. 2.6 [15].

2.2.3 Field Propagation Equation

The propagation equation for a field envelope derived using Maxwell's law depends on the polarization it excites in the medium in which it is travelling. Thus the equation for the probe and the control fields are given by:

$$(\partial_t + c\partial_z) \alpha(z, t) = i \frac{\omega_1}{2\epsilon_0} \frac{N}{V} \wp_{eg} \tilde{\rho}_{eg}(z, t) \quad (2.23)$$

$$(\partial_t + c\partial_z) \Omega(z, t) = i \frac{\omega_2}{2\epsilon_0} \frac{N}{V} \wp_{es} \tilde{\rho}_{es}(z, t) = 0 \quad (2.24)$$

Eqn (2.24) is the celebrated undepleted pump approximation. We define the optical polarization $P(z, t) = \sqrt{N} \tilde{\rho}_{eg}(z, t)$ and the collective spin wave of the atomic ensemble $S(z, t) = \sqrt{N} \tilde{\rho}_{sg}(z, t)$, where N is the number of atoms in the interaction region of volume V . We define $g\sqrt{N} = \wp_{eg} \sqrt{\frac{\omega N}{2\hbar\epsilon_0 V}}$ as the collectively enhanced coupling constant between the signal field and the atomic medium, and redefine the signal field amplitude as $\mathcal{E} \equiv \mathcal{E}_1 \wp_{eg} / (g\hbar)$. Under these approximations, the three equations that govern signal (probe light) propagation and the atomic response are:

$$(\partial_t + c\partial_z) \mathcal{E}(z, t) = ig\sqrt{N}P(z, t) \quad (2.25)$$

$$\partial_t P(z, t) = -[\gamma - i(\Delta + \delta)]P(z, t) + i\Omega(z, t)S(z, t) + ig\sqrt{N}\mathcal{E}(z, t) \quad (2.26)$$

$$\partial_t S(z, t) = -(\gamma_0 - i\delta)S(z, t) + i\Omega^*(z, t)P(z, t) \quad (2.27)$$

Solving the equations after taking Fourier transform, and using the relation of induced polarization:

$$P_{\text{ind.}}(\omega) = N \langle g | \hat{\mathbf{e}}_1 \cdot \mathbf{d} | e \rangle \tilde{\rho}_{eg}(\omega) = \epsilon_0 \chi(\omega) E(\omega),$$

we find the following expression for the electric susceptibility, $\chi(\omega)$ of the medium:

$$\chi(\omega) = \frac{N\wp_{eg}^2}{V\epsilon_0\hbar} \frac{\delta + \omega + i\gamma_0}{|\Omega(z)|^2 + \Gamma_0\Gamma}. \quad (2.28)$$

where,

$$\Gamma_0 \equiv [\gamma_0 - i(\delta + \omega)], \Gamma \equiv [\gamma - i(\Delta + \delta + \omega)]$$

The complex refractive index of a medium depends on χ as

$$n = \sqrt{1 + \chi} \approx 1 + \frac{\chi}{2}$$

$$\tilde{n}(\delta) \approx 1 + \frac{d/Lc\gamma}{\nu_1|\Omega(z)|^2} \left(\delta + i \frac{\gamma\delta^2}{|\Omega(z)|^2} + \mathcal{O}(\delta^3) \right) \quad (2.29)$$

2.3 EIT with zero detuning of control

The transmission curve is generally plotted to observe the EIT window, while the dispersion profile is plotted to observe the steep variation in the slope of the refractive index of the medium. The transmission of the signal is proportional to the $Im[\rho_{eg}]$ and the refractive index (dispersion profile) is proportional to the $Re[\rho_{eg}]$, and are plotted in the figure (2.6). When the control is turned off, the transmission curve changes to the grey-dashed line, the grey-dashed line represents the transmission and dispersion of a probe in the case of a two-level system.

The curve follows the solid line when the control field is turned on and is resonant ($\Delta = 0$) to the $e \leftrightarrow s$ transition. The presence of the control field renders the medium transparent for the probe field due to the quantum interference between the fields[15]. The width of the window of transparency depends on the Rabi frequency of the control field, and the Rabi frequency is proportional to the intensity of the electromagnetic field (Eqn (2.8)). This essentially means that as we increase the intensity of the control field, the window's width widens[19][4]. The transmission window allows a certain probe bandwidth to pass through the atomic vapor. The bandwidth of the probe corresponds to the width of the window. The probe transmission is maximum at the peak of the transmission window, i.e., when the probe is at resonance.

2.4 EIT with Off-Resonant Control Field

Let us detune the control field and observe its effect on the transmission curve 2.6. We can see clearly from the curve that as we increase the detuning of the control field, the peak is shifted, and the symmetry is distorted.

We need to look at the EIT window with off-resonant control field because in our system, the AOMs introduce a frequency shift equal to its driving frequency which is in the range of 80 – 130 MHz. The transmission and refractive index curves for such a highly detuned control fields are shown in the figure 2.6.

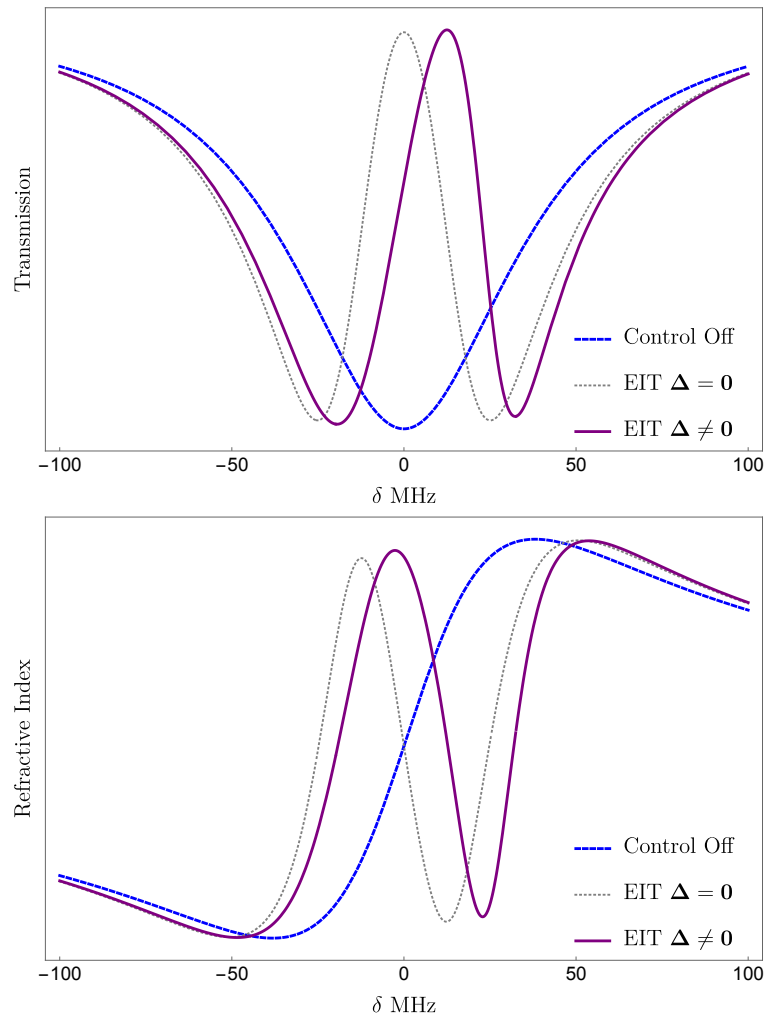


FIGURE 2.6: Use figure with detuning = 100 MHz (Top) Transmission vs detuning and Refractive index vs detuning of probe beam is plotted when the control is OFF (dashed, blue), control is ON and $\Delta = 0$ (dotted, gray), and control is ON and $\Delta \neq 0$ (solid, purple).

2.5 Slowing of Light

The complex refractive index in Eq. (2.29) varies rapidly around the resonance. Since, the group velocity of the signal field depends on the complex refractive index, the group velocity must also change. Thus, we can write:

$$v_g = \frac{c}{n(\omega) + \omega \frac{dn}{d\omega}}.$$

We see from the expression for the complex refractive index in Eq. (2.29), that

$$\begin{aligned} n_g &= n + \nu_1 \frac{dn}{d\nu_1} = n + \nu_1 \frac{dn}{d\delta} \\ &\approx 1 + \frac{d\gamma c \delta}{\nu_1 L |\Omega|^2} + \frac{d\gamma c}{L |\Omega|^2} \end{aligned}$$

Near the resonance $\delta = 0$, n_g is dominated by the third term, so that the group velocity experienced by a pulsed signal field is

$$v_g = c/n_g \approx \frac{|\Omega|^2 L}{\gamma d} \quad (2.30)$$

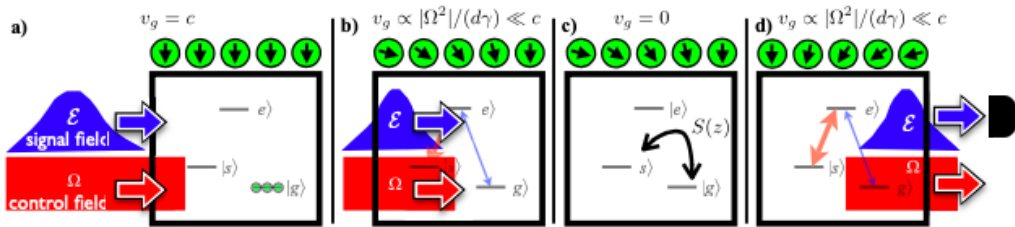


FIGURE 2.7: (a)The control field (red) optically pumps all of the atoms (green dots) into the ground state $|g\rangle$ Before the EIT medium, the signal pulse (blue) propagates with $v_g \approx c$. (b) The intensity of the control field remains constant. Upon entering the cell, the signal pulse experiences a reduced $v_g \ll c$, causing the signal pulse to spatially compress. An atomic spin wave is created along the cell in the direction of the pulse propagation, as illustrated by the rotated atomic spins. (c) When most of the signal pulse is inside the cell, the control field is extinguished, which sends $v_g = 0$, and maps any information encoded in the signal pulse onto the spin wave. (d) After a prescribed amount of time, the control field is turned on, releasing the spin wave into the signal field, which leaves the cell.

Thus we see that the group velocity of the signal field can be slowed down and stopped by decreasing the Rabi frequency of the control field to 0 or in simple terms by decreasing the intensity of the control field to zero. The stopping of light means

that the signal pulse has been stored in the atomic coherence ρ_{es} .

Mathematical equations suggest that the control field can be turned back ON to re-accelerate the stopped pulse. However, the retrieval is time bound due to the decoherence of the storage state ($|s\rangle$). Therefore, the storage time of the signal pulse is limited.

We have performed a numerical simulation of Eqs. (2.25), (2.26), (2.27) to show the storage time vs efficiency curve of a EIT based QM. The more storage time we have, the less efficient the QM becomes.

Chapter 3

Basic Experiments

3.1 Spot Size Measurement

Measuring the height of the beams used in the experiment as well as their spot size is the first step to complete in any experiment. In order to perform the experiment accurately, the height of the beam as well as its spot size should be constant throughout the experimental setup.

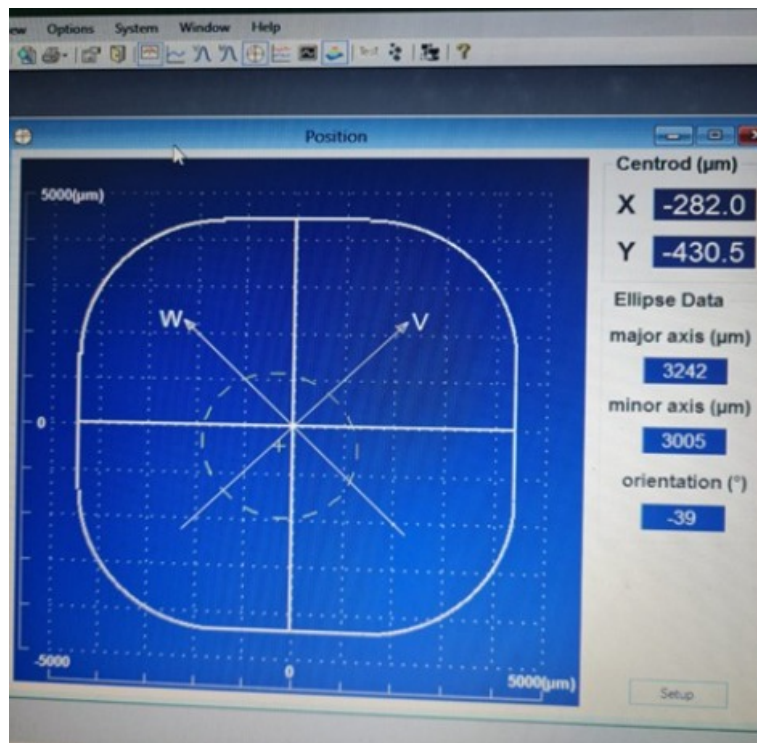


FIGURE 3.1: You can see the measurements for the semi-major and semi-minor axes of the spot size. You can also observe where the beam falls on the CBM's window and how far it is from the centre

In most of the experimental setups, the beam coming from the output port of the laser is reflected to the experimental setup using a mirror. In order to set the height

properly such that it stays constant throughout the experimental setup, we need to perfectly calibrate the mirror. For measuring the height, take the scale and place it a few inches away from the mirror, and take the reading. Make sure you notice where the centre of the spot made by the beam on the scale is. Now keep the scale farther away, and take the reading again. If there is a change in the reading, calibrate the mirror by moving the knobs on its kinematic mount such that the height at this distance (of the centre of the spot made by the beam on the scale) is the same as the height you measured earlier. Repeat this for an even farther distance just to be sure.

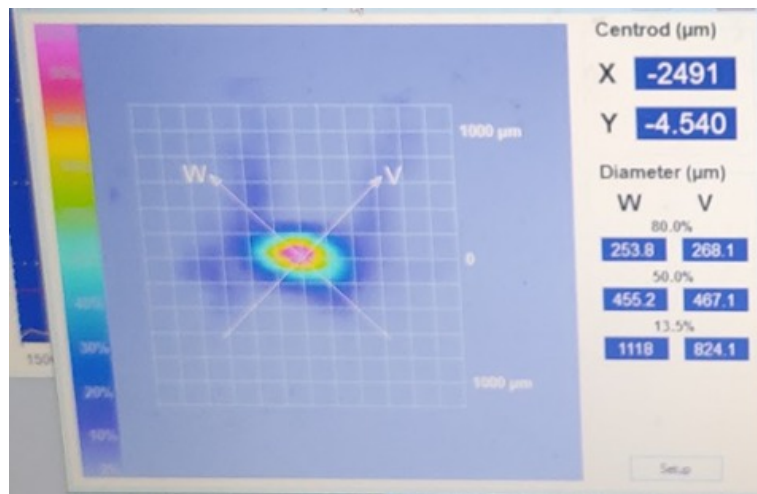


FIGURE 3.2: This is how the heat profile (heat map) will be displayed on the software. This lets us know how uniformly the power is distributed in the beam.

Now that you have calibrated the height, you need to make sure the light is travelling in a straight line along the optical table, i.e. its path isn't slant. Repeat the process described above, but instead of checking the height, check the lateral movement of the beam.

Now that the beam's height and lateral degree of freedom have been calibrated, we need to measure the spot size. This can be done approximately by checking whether the spot made on the scale by the beam is changing or not, i.e. if it is converging or diverging. This can be done by keeping the scale at different distances and checking the shape and size of the spot made on the scale.

In order to measure the spot size accurately, we use the Coherent Beam Master (CBM). Take off the cover from the CBM's input window and place it in front of the beam such that the beam falls on the window perfectly. Connect the CBM to a laptop

which has the necessary software. Now you can observe the spot size, it's shape and it's heat map. Take the reading of the semi-major and semi-minor axes shown on the screen.

3.2 SAS

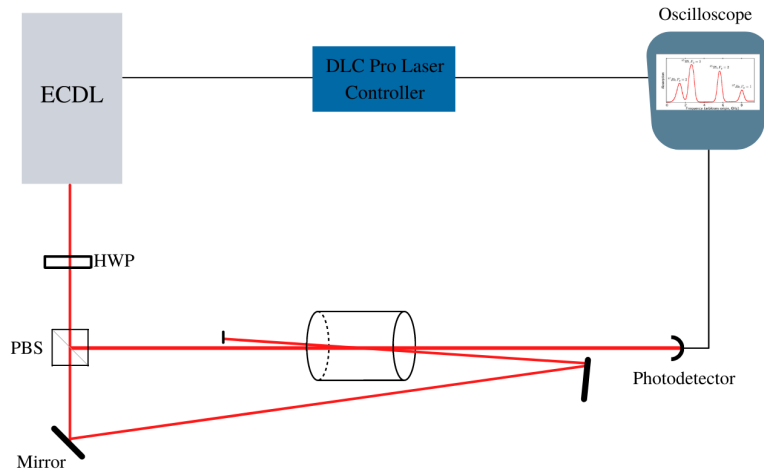


FIGURE 3.3: Experimental setup of SAS performed in our lab. Notice that we have used only overlap beam for this purpose. DLC Pro controller is used to lock the laser at any peak in the spectrum observed on the oscilloscope.

In the lab, we modified our SAS setup based on our needs. We removed the reference beam while the rest of the setup was kept intact. We observed the signal with a single photodetector. The difference between the observed spectrum and the proposed spectrum in the theory section is that in theory, we subtract the observed signal with the doppler broadened spectrum to get Doppler-free spectra. Here, we do not subtract and observe the signal as it is. We observe that the rubidium spectra overlapped on a doppler broadened profile. The peaks we observe in the spectra are of significance. We determine the peak-to-peak frequency gap by overlapping the spectra with the 1 GHz Fabry-Perot spectrum. We use the FPI spectrum like a scale to measure the frequency gap.

The SAS spectrum for Rubidium is shown in the figure below. The dominant

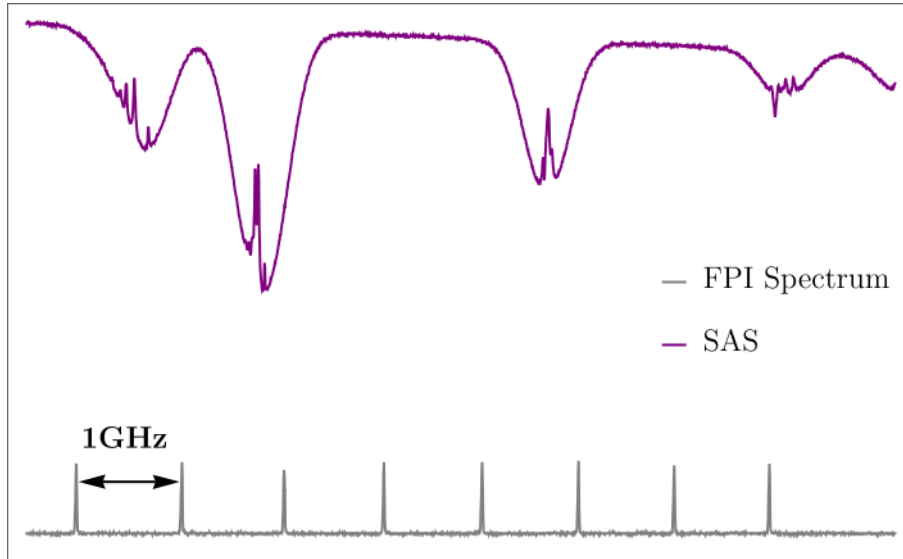


FIGURE 3.4: Hyperfine spectrum of Rubidium collected from our experimental setup. The Fabry-Perot spectrum acts as a scale to measure the frequencies of the HF spectra. The separation of 6.8 GHz between the ground states is roughly verified by the plot.

peaks correspond to ^{85}Rb , while the slightly weaker peaks correspond to ^{87}Rb . Left-most peaks are for ^{87}Rb , $F = 2$ to $F = 1 - 3$ transitions. The second peak from the left is for ^{85}Rb , $F = 3$ to $F = 2 - 4$. The third peak is for ^{85}Rb $F = 2$ to $F = 1 - 3$. The rightmost peaks correspond to ^{87}Rb , $F = 1$ to $F = 0 - 2$ transitions. We use mainly ^{87}Rb $F = 2$ to $F = 1, 2$ and $F = 1$ to $F = 1, 2$ transitions in our experiments on EIT.

3.3 Laser Locking

Laser locking using the touchscreen of the DLC Pro Module is performed as follows:

- Step 1: Obtain the spectroscopy profile on the DLC Pro Module screen
- Step 2: Click on the button depicted by a "lock on a spectrum". Circles (without a border) enclosing the peaks and dips will now be visible on the screen. If you are not able to see the peak/dip at which you want to lock the laser, try changing the Scan Amplitude, the Set Current and the Scan Offset to bring the peak/dip you want to lock on the centre of the screen.
- Step 3: Tap gently on the peak/dip you want to lock the laser at. This may take a few attempts. Finally, the peak/dip you want to lock the laser at will be enclosed (with a colored border) within a circle.

Step 4: Once you are satisfied with your selection and are sure the centre of the circle is at the peak/dip, press the button depicted by only a "lock". Your laser is now locked at the required peak/dip (frequency).

3.4 Phase locking of probe and Control field

Consider, suppose, a three-level system, with a probe field frequency at the $5^2S_{1/2}F = 1 \rightarrow 5^2P_{1/2}F' = 1$ and with a control field frequency at the $5^2S_{1/2}F = 2 \rightarrow 5^2P_{1/2}F' = 1$. Using the Toptica CoSy Module, we can lock the control field at the frequency described above, after which we phase-lock the probe field to always transmit light at exactly 6.8348 GHz (difference between the two hyperfine levels) away from the probe laser. This will be achieved with the FALCpro module by Toptica.

3.5 Observation of EIT Window

The experimental setup for observing the EIT window is shown below.

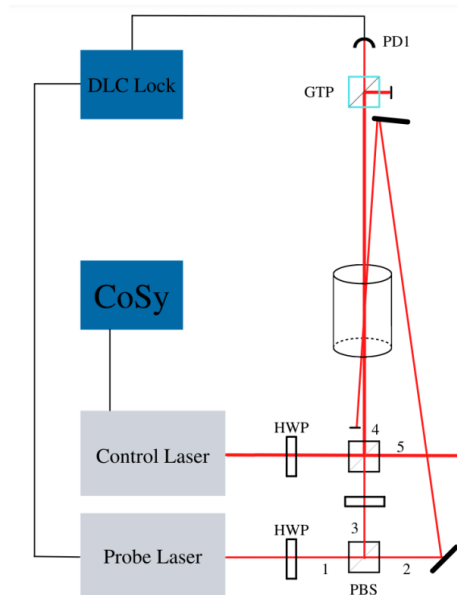


FIGURE 3.5: HWP-Half Wave Plate, PBS - Polarizing Beam Splitter, GTP - Glan Taylor Polarizer, PD - Photodetector, CoSy - Compact Spectroscopy

The cylinder in between is the Rb vapor cell, which can also be enclosed in a Gauss Chamber. The above setup is for the experiment of EIT with SAS. The HWP+PBS combination is used to control the power of control and probe beams.

The HWP rotates the polarization, which in turn rotates the amount of horizontal and vertical polarization the field has. The PBS separates out these polarizations, and hence their combination can be used to control the power in a specific polarization (horizontal or vertical) according to where the said polarization might travel in the experimental setup.

The HWP along '3' is used to rotate the polarization of the reflected vertically polarized probe beam such that a part of it is transmitted through the second PBS. The control field is denoted with dark red color whereas the probe field is denoted with light red color indicating the intensity of the beams. .

Make sure that the height of all the beams is the same throughout the experimental setup and that there is no deviation (slant) (Section 3.1). This will make it easier to overlap the control and probe beams. The control and the probe beams should completely overlap for the whole path to the GTP to get the best absorption EIT peak. If this cannot be achieved precisely, it is enough if the two overlap inside the Rb cell. Aligning the first PBS so that the probe passes correctly through the second PBS, and then altering the orientation of the second PBS is an efficient way to make the two beams overlap.

The control, the probe and the pump beams interact in the vapor cell. Using a GTP, we remove the control beam, and the probe beam proceeds to the photodetector. The signal from the photodetector is fed to another DLC Pro Locking module, which also controls the ECDL. We use the DLC Pro module to scan the laser by applying a time varying current and voltage to the piezo transducer of the ECDL. Now lock the control beam using the CoSy module at the frequency you want by following the steps given in Section 3.3.

Once the setup is complete with the overlap, remove the Rb vapor cell. Use the Coherent Beam Master (CBM) to measure the spot size (i.e., the dimensions) (Section 3.1) of the control and the probe field. Keep the CBM window at approximately the same position where the fields enter the vapor cell. Note down the dimensions. Next, measure the power of both the fields using the power meter. This is used to calculate the intensity of both the fields and hence the Rabi frequencies of both the fields.

Notice the probe field going along path '5'. This can be guided towards a Fabry

Perot Interferometer (FPI) in order to convert time into frequency and will be used to calibrate the time axis of the spectrum. This is done for the purpose of analysing the spectrum and its FWHM in terms of frequencies. Now take the data from the oscilloscope in a USB drive which shows both the EIT window as well as the output from the FPI and store it in your PC. Analyse the data in MATLAB to calculate the FWHM of the EIT peak.

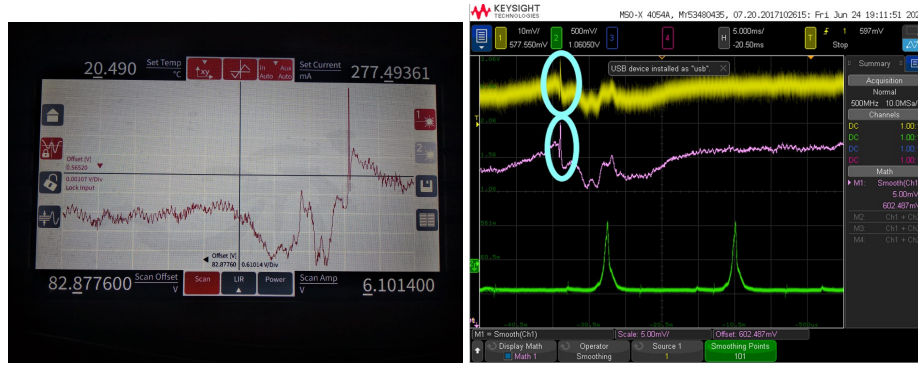


FIGURE 3.6: EIT window as observed in the DLC Pro module (left) and on the Oscilloscope (right) (yellow) with the smoothed curve (in purple) and the FPI output (green). The EIT windows have been circled.

The SAS setup does not influence the EIT window. Even without SAS, the EIT window obtained will be the same as it will be with SAS. This can simply be checked by blocking the probe field which was reflected from the mirror (path '2') and observing the change on the oscilloscope.

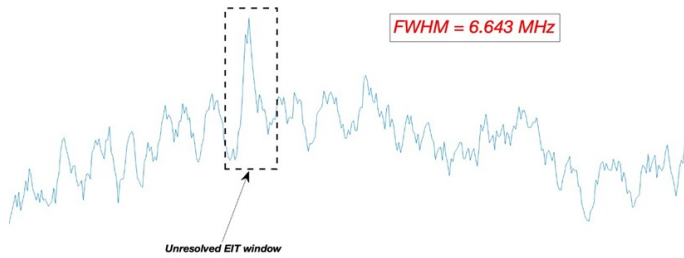


FIGURE 3.7: Data from the oscilloscope as plotted in MATLAB. The FWHM has been calculated to be 6.643 MHz, which is in agreement with previously published papers and theoretical predictions.

3.6 Pulse generation using AOM

3.6.1 AOM alignment

The optical bench alignment of an AOM requires effort. The key parameters of focus include the angle of incidence based on our requirement, whether we need to upshift or downshift the optical frequency; the RF driving frequency; the size of the beam near the aperture of the AOM because its response time depends on the diameter of the incident beam; and the intensity of the optical beam so that we can observe the first-order beam with ease. We adjust the height, slowly rotate the AOM to a convenient position, and then move the mirror from which the optical beam is reflected to fall on the AOM. We stop moving the knob of the mirror when we distinguish the first-order beam from the zeroth-order.

3.6.2 Frequency Shift

We also measured the shift in the frequency of the first-order beam. The beam is coupled to an optical fiber. The beam is incident on the input port, and the fiber out was kept in front of a CCD camera. Once the beam is visible on the camera's display, we connect the output to the wavelength meter and note down the frequency. The frequency of the 0th order beam was measured and then subtracted from the frequency of the first-order beam. This shift in frequency, in theory, should be equal to the RF reference frequency in the range of 80 MHz - 133MHz.

3.6.3 Delay, Rise, and Fall time of AOM

To observe the delay, rise, and fall time of an AOM, we modulate the RF driver with a digital input sequence via Data Acquisition (DAQ) module (PXIE-6363) using the NI LabVIEW interface. We simultaneously input the modulated digital signal from the RF driver with the detected signal from the output port of the AOM. We zoom into the oscilloscope up to the nanosecond scale and visualize the plots' delay, rise, and fall time. The plots are shown in the figure below, and their analysis shows that the rise and fall times are roughly 150 ns while the delay is around $1.1\mu s$.

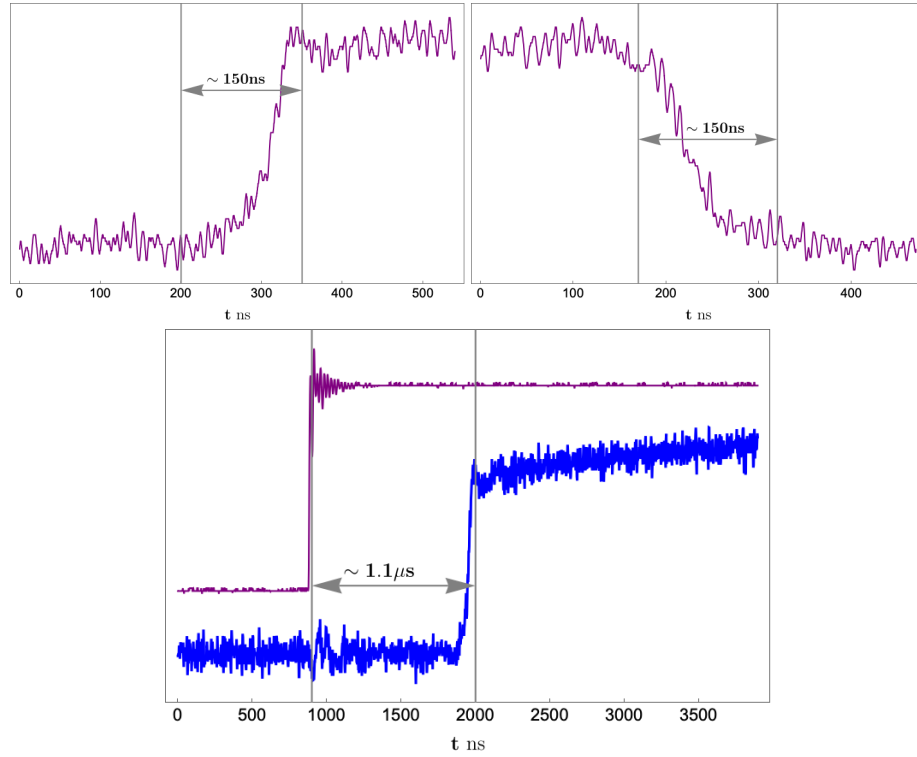


FIGURE 3.8: Experimentally measured rise time (top left) and fall time (top right) of an AOM, and delay (bottom) between the input(purple) amplitude modulated signal and the AOM output(blue).

3.6.4 Amplitude Modulation

Our experiment requires light pulses of arbitrary shapes such as Gaussian pulses, square pulses, etc. So, we need to modulate the RF driver to output these arbitrary waveforms. The RF driver has an input port for amplitude modulation, where we can input a modulating signal, which will modulate a reference frequency (80 MHz - 133 MHz) and give out an amplitude modulated signal. We can produce customized shapes of the waveform in this way. The amplitude modulated signal is then fed to the AOM, and the pulses of light are detected on the photodetector. The figure shows that the AM signal and the detected signals are compared on the oscilloscope. The figure depicts the issue regarding the high rise and fall time of the AOM. Also, the delay is visible on this time scale.

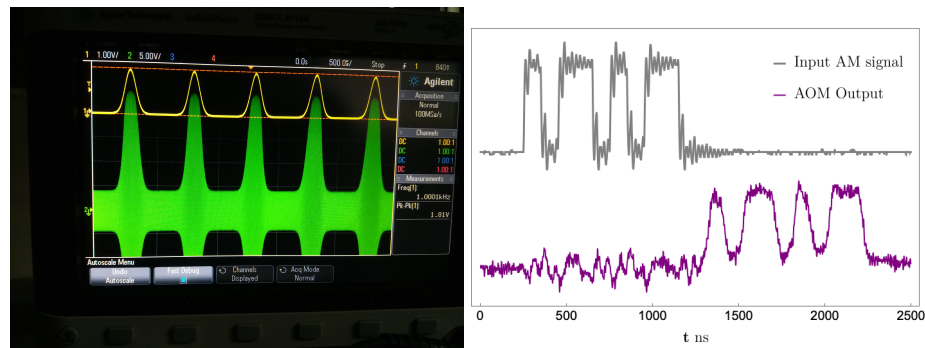


FIGURE 3.9: Left figure - Yellow is the input waveform for amplitude modulation. Green is the amplitude modulated output from the RF driver. Right figure - Gray is the amplitude modulated signal form the RF driver. Purple is the corresponding AOM output, with a delay and distortion due to the limitation of the rise and the fall time of the AOM.

Chapter 4

Quantum Memory

4.1 Laser Preparation

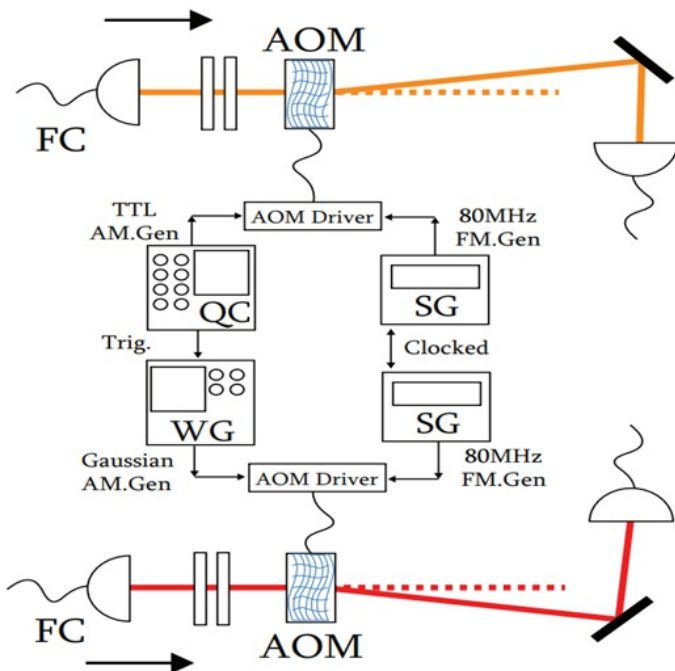


FIGURE 4.1: Input Preparation for Probe and Control Pulses

The above setup will be responsible for pulse creation of both control (orange) and probe (red) and encoding the polarization qubit. Single photon pulses for probe beam will be created by adding an attenuator after the AOM. FC is the Fiber Coupler which outputs the beam. Direction of the arrow indicates the direction of the laser. Here we have a QC (Quantum Composer QC9520 series), which will act as a trigger for all the other components. WG and SG are the Waveform Generator and the Signal Generator respectively.

The QC will trigger the WG (Tektronix, SN: AFG3051C), and with every trigger, the WG will produce a Gaussian peak with an FWHM of 400 ns or 25MHz. This will be used as AM for the AOM Driver, and will be used to create and shape the probe pulses. The QC has two types of outputs, TTL/CMOS or voltage adjustable output. TTL stands for Transistor- Transistor Logic. Suppose the voltage is between x V and y V, the TTL will be 1, and AM will be given to the AOM driver attached to the AOM in the path of the control pulse. If the voltage is below y V, the TTL will be 0, and no AM will be given to the AOM driver. This means that whenever the TTL is 1, AM will be given only at those instants, and this will lead to formation of pulses for the control field.

Instead of using the internal mechanism of the RF driver for changing the frequency of the incoming beam, Namazi[27] used an external source, the SG (Agilent SN: 33250A) to provide the necessary detuning (corresponding to the single photon detuning) of ± 80 MHz to the probe and control fields. They have termed this as Frequency Modulation (FM). This is different from the FM that we provide externally to the RF driver. For Namazi[27], FM means altering the frequency of the beam. Reference: “Commercial AOM drivers are typically equipped with an internal local oscillator to generate the frequency modulation (FM) to the amplifier.”- M. Namazi[27](Pg 43). The “Clocked” written between the 2 SGs refers to clocking/synchronization for them. The “Clock-in” functionality of the QC gives the user the ability to synchronize using a master clock from 10 to 100 MHz. This will be used to synchronize them.

It depends on us what order of detuning we want, (+1 or -1 order), and accordingly we can set the AOM and the mirrors. The beam/ pulses created will be sent to the FC for the main experiment. The waveplates used are for encoding the polarization qubit. The final qubits are then sent to the quantum memory through single-mode non-polarization-maintaining optical fibers.

4.2 Pulse Synchronization

A pulse delay generator (for eg. the aforementioned Quantum Composer) will be used to synchronize the probe and control pulses. This will be done in an iterative

manner, meaning the delay generated by the pulse delay generator will be changed continuously by our observation of the delay between the probe and the control pulses.

4.3 Qubit Encoding & Decoding

4.3.1 Polarization Encoding

We know that we can have a qubit in two distinguishable, i.e., orthogonal states $|0\rangle$ and $|1\rangle$. A qubit can be encoded in many degrees of freedom of a photon, and here we are focusing on the polarization degree of freedom [30], where a photonic qubit can be defined as:

$$\begin{aligned} |0\rangle &= |H\rangle \\ |1\rangle &= |V\rangle \end{aligned} \tag{4.1}$$

Where $|H\rangle$ denotes horizontal polarization and $|V\rangle$ denotes vertical polarization. In this case, arbitrary qubit states can be $\alpha_0|H\rangle + \alpha_1|V\rangle$. Polarization qubits can easily be created and manipulated with high precision by simple linear-optical elements such as polarizing beam splitters (PBS), polarizers, and wave plates. Polarization encoding can be done using a combination of optical waveplates. Setting their angles will get the job done.

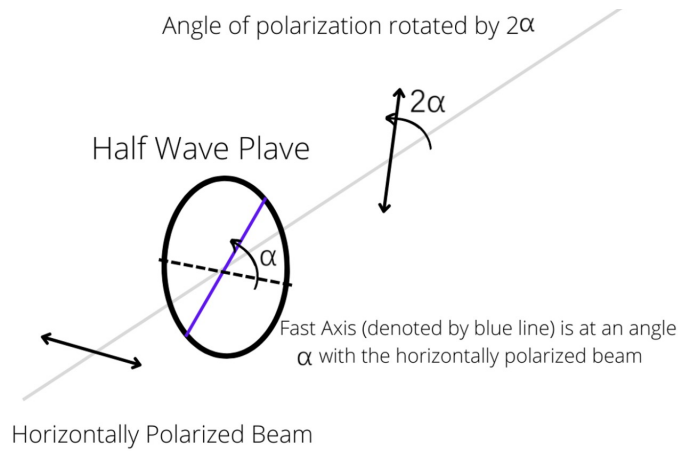


FIGURE 4.2: Polarization Encoding Using a HWP

As shown in Fig 4.2, the initial polarization $|H\rangle$ is rotated to a superposition described by $\cos 2\alpha|H\rangle + \sin 2\alpha|V\rangle$.

Decoding the polarization can be done by using a PBS to separate out the horizontal or vertical components in case of a CW laser. In case of a photon, repeated measurements (known as ‘shots’ in the Qiskit language) have to be made in order to compute the value of α and hence the amplitude of $|H\rangle$ given by $\cos 2\alpha$ and the amplitude of $|V\rangle$ denoted by $\sin 2\alpha$.

4.3.2 Time-Bin Encoding

This concept is used to encode the qubits as time-bins [6], which is essentially using the concept of arrival time of the qubit or the path length taken by the qubit to form our basis. This becomes clearer in the reference of an unbalanced Mach-Zehnder interferometer (MZI), where one arm is longer than the other. The unbalanced MZI is shown as[11]:

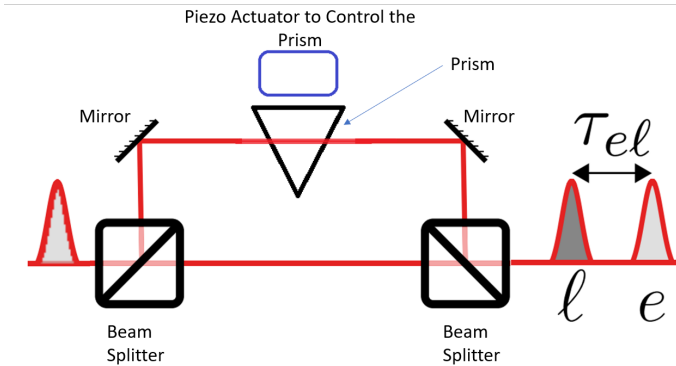


FIGURE 4.3: Unbalanced MZI with Prism

We see a single pulse going through the beginning of the MZI, which will get divided into two pulses due to the BS at the beginning of the MZI. One will take the longer (upper) path and the other one will take the shorter (lower) path. represents another shift in the length, hence in the phase, which is controlled by a prism that can alter the time the light pulse travels inside the prism. The prism is controlled by a piezo actuator which will be used to vary the position of the prism and hence control the amount of time the beam is passing through the prism, leading to an extra time lag between the two pulses $|early\rangle$ and $|late\rangle$.

Another BS is used at the end to combine these two pulses, and we get a time lag of δt between them.

This can be applied to the case of a single photon as well, where after passing the first BS, the photon will be in a superposition of $|early\rangle$ (denoted by 'e' in the figure above) (or $|short\rangle$) and $|late\rangle$ (denoted by 'l' in the figure above) (or $|long\rangle$), given as $\alpha_0|short\rangle + \alpha_1|long\rangle$. By calculating the time taken by the photon to get to the detector from both the parts, we can check whether we have a $|short\rangle$ or a $|long\rangle$ time bin. τ_{el} is the time difference between them.

The time of arrival as seen in the SPCM can give us the result of whether the outcome is a $|early\rangle$ or a $|late\rangle$. Repeated measurements have to be done in order to get the amplitudes (or probabilities).

4.4 Storage & Retrieval

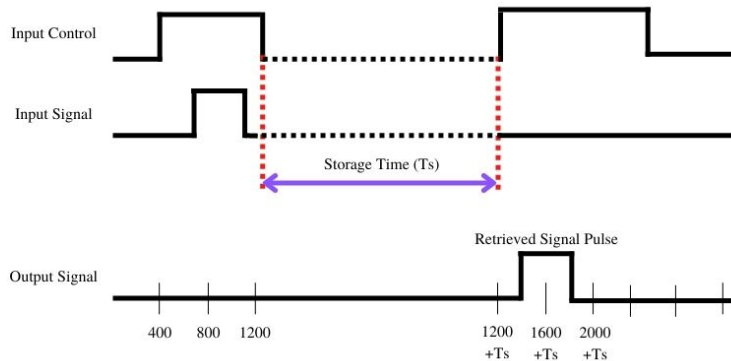


FIGURE 4.4: Timing Diagram of Control and Probe Pulses (The time scale is in ns.)

In the storage process, we send the signal and the control pulses together in the storage cell such that the end of both the pulses are synchronised. This is done to prevent the retrieval of the signal pulse before the storage process ends. Another control pulse is sent to the cell after a storage time T_s to retrieve the signal pulse. Refer to the timing diagram fig. to see when the pulses are triggered. The control pulses is kept longer so that it temporally overlaps the signal pulse. However, the control and the probe pulses and their timing can be optimized to improve the storage performance.

4.5 Detection

4.5.1 Semi-Classical Pulse

For this, the detection will be done using a fast photodiode, and the output will be read on the oscilloscope.

4.5.2 Single-Photon Pulse

Time-Correlated Single Photon Counting [13] - or TCSPC - is based on the detection of single photons of a periodical light signal, the measurement of the detection times of the individual photons and the reconstruction of the waveform from the individual time measurement. The method makes use of the fact that for low level, high repetition rate signals the light intensity is usually so low that the probability to detect one photon in one signal period is much less than one. Therefore, the detection of several photons can be neglected and the principle shown in fig. 2 right be used: The detector signal consists of a train of randomly distributed pulses due to the detection of the individual photons. There are many signal periods without photons, other signal periods contain one photon pulse. Periods with more than one photons are very unlikely. When a photon is detected, the time of the corresponding detector pulse is measured. The events are collected in a memory by adding a '1' in a memory location with an address proportional to the detection time. After many photons, in the memory the histogram of the detection times, i.e. the waveform of the optical pulse builds up.

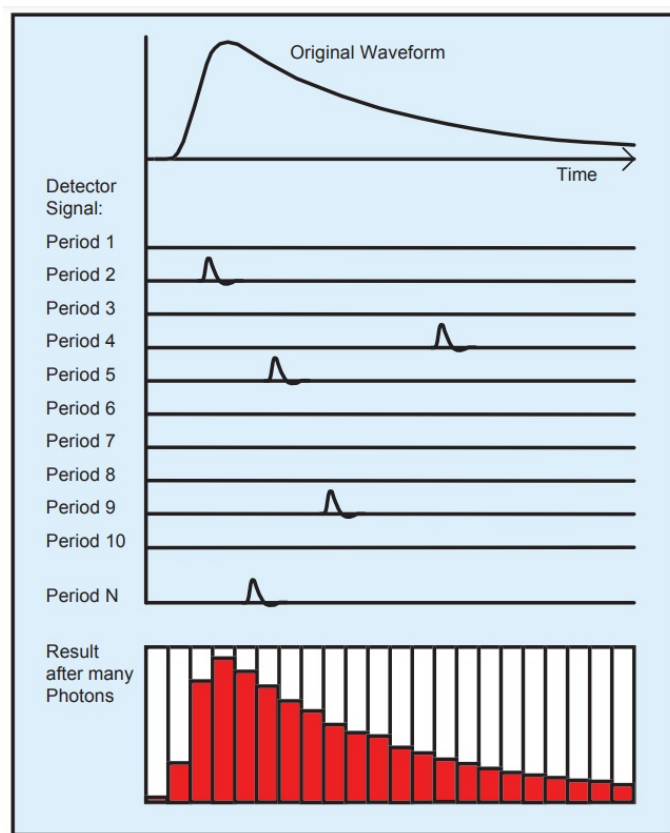


FIGURE 4.5: Principle of the TCSPC technique [13]

Chapter 5

Frequency Filtering

The current, to be implemented, setup accounts for both frequency and polarisation correction. Two etalons (Fabry-Perot-Interferometers) act as a frequency filter. To further separate the control field from the probe, we implement filtering based on its frequency. (Reference for above set up is here[27])

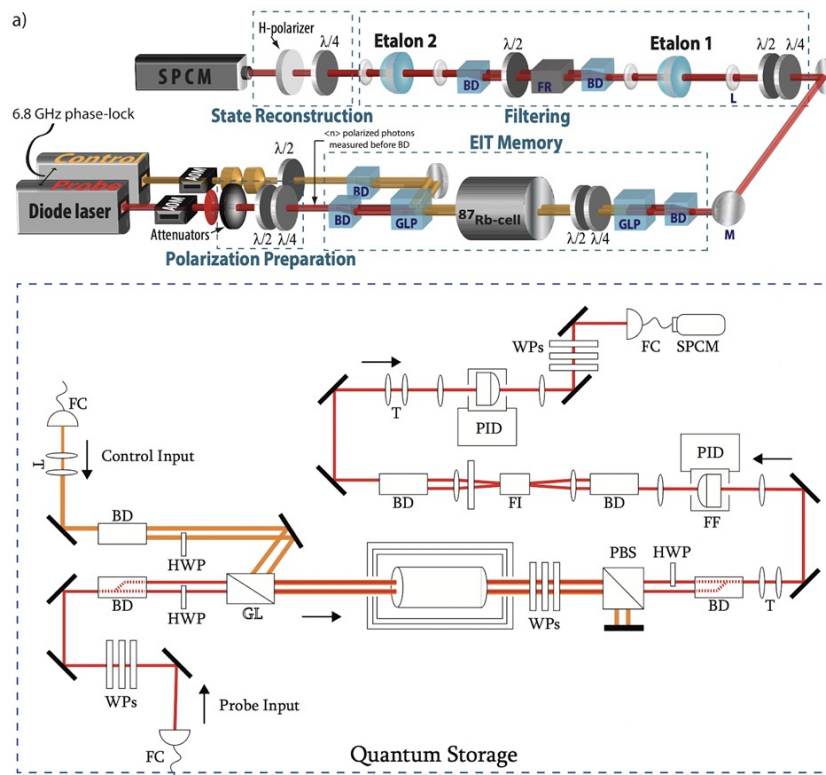


FIGURE 5.1: Frequency Filtering Setups

Here as shown in the diagram after retrieving the qubit (information encoded in the polarisation of a photon) from the memory part it goes into the filtering unit.

Fabry-Perot Resonator: They are a kind of open resonators, which in simple words allow frequencies resonant with the cavity to pass through them and block

the rest. Hence they can be used as a frequency filter. Fabry-Perot Interferometers are sensitive to temperature and hence a feedback system, in the form of a PID controller is used to maintain the temperature up to a precision of 0.01K. Lenses are used to focus beams onto different optical elements like etalons, beam displacers, and Faraday rotators.

5.1 Etalons

Dual Etalons: In optical systems, components are used in series as light passes from the output of one component to the input of the next. In such optical chains, the transmission profiles of each element are multiplied to obtain the final system transmission profile. As such, two etalons may be used in series to further limit the transmission of light through the system.

Essentially the wavelength (or frequency) transmission from a series combination of etalons will be much more fine with increased Finesse.

(Reference for numerical analysis of dual etalons is here[23])

Another important thing to be kept in mind during the set up of this unit is mode matching by adjusting the mirrors in order to use the laser more judiciously. The wavefront of the beam prior to entering the etalons needs to be matched accordingly to the wavefront in the etalons (gaussian profile). Choosing the characteristics of FPI mirrors becomes important to eliminate minute errors to have ideal outputs. The use of lenses is primarily for this purpose[3].

5.2 Faraday Rotators

5.2.1 Faraday Isolator

A problem with using FPRs in series is the reflections from 2nd etalon may interfere with the 1st etalon, for this reason we need a way to block the reflections.

This is done by incorporating the Faraday Rotator in between the two etalons. Optical isolators are different from 1/4 wave plate based isolators because the Faraday rotator provides non-reciprocal rotation while maintaining linear polarisation. That is, the polarization rotation due to the Faraday rotator is always in the same

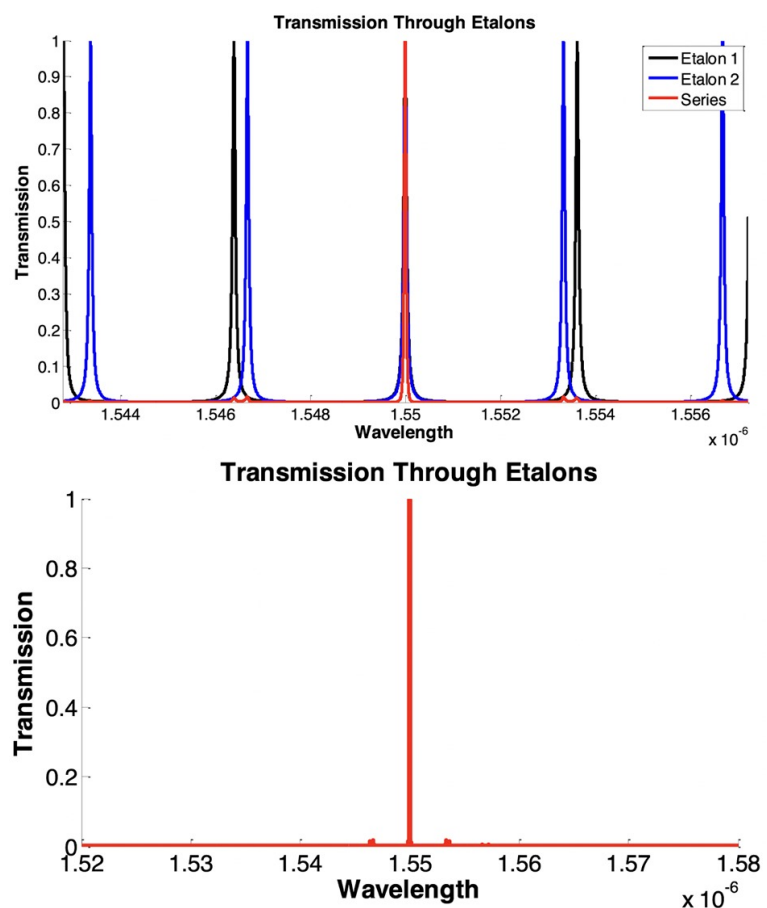


FIGURE 5.2: Transmission profiles (w.r.t wavelength) from the two etalons (Left). Overall transmission from the series combination of the two etalons (Right)

relative direction. So, in the forward direction, the rotation is positive 45° . In the reverse direction, the rotation is 45° . This is due to the change in the relative magnetic field direction, positive one way, negative the other. Conventional FIs induce a 90-degree of polarization rotation between the forward and backward beams and deflect the backward beams using two PBSs. Due to the use of PBSs, these isolators are polarisation selective which goes against the nature of our quantum memory. To avoid this issue, the two PBSs are replaced with two BDs.

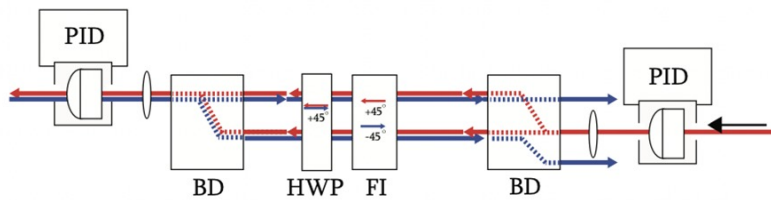


FIGURE 5.3: Diagram depicting overall working of the Faraday Rotator. FI stands for Faraday Isolator

Its functioning is clearly understood with the above diagram where the red and blue beams represent forward and backward propagating light.

Refer here[28] for component specifications and use.

Another important thing to note is that the HWP between the FI and 2^{nd} BD, besides rotating the reflected beam also corrects the polarisation swapping done by HWPs in the earlier part of the setup.

5.3 Longpass Filter

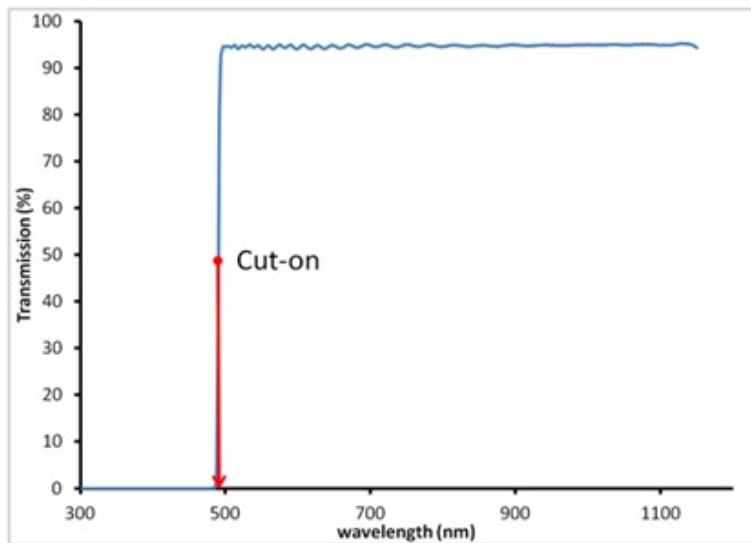


FIGURE 5.4

Longpass filters [29] (sometimes called edge filters) transmit wavelengths above (LP) a certain wavelength. This wavelength is called the cut-on wavelength for long-pass filters. The cut-on wavelength designates the wavelength at 50% of the peak transmission as shown in Fig. 5.4 (the rising edge for a LP). We can see in the Fig. 5.4 that wavelengths above 500 nm (approximately) will be allowed to pass through the longpass filters.

5.4 Bandpass Filter

An optical bandpass filter [14] is a spectrally selectively transparent component capable of transmitting select wavelengths of light over a range while blocking others. For example, a visible optical bandpass filter would operate within the visible spectrum, passing wavelengths between 380 – 780 nm. Ultraviolet optical bandpass filters can eliminate all visible light and near infrared radiation to transmit wavelengths of below 380 nm – while near-infrared filters are passing near-infrared radiation of close to 780 – 2,500 nm.

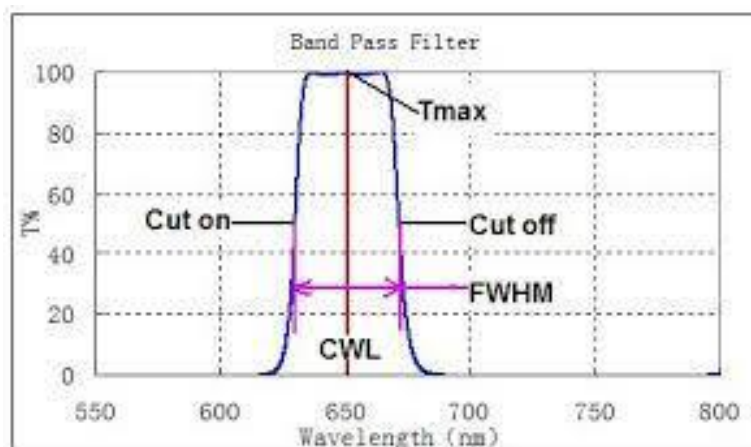


FIGURE 5.5: Working of an optical bandpass filter. CWL stands for Central Wavelength

Chapter 6

Introduction and Theory of Quantum Frequency Conversion

The thesis work revolves around light-matter interactions and their experiments. We have demonstrated EIT in a Λ type atomic system at different probe and control powers. We have also performed EIT in the presence of a magnetic field. The theory of EIT is slightly modified by considering a slight detuning of the control field. The behavior of the probe is then observed. Then we conclude that the system can act like a three-level optical switch depending on the detuning of the probe relative to the control field frequency. The results of the experiment are shown in the experiment and results section.

6.1 Introduction

Quantum frequency conversion (QFC), a critical technology in photonic quantum information science, requires that the quantum characteristics of the frequency-converted photon must be the same as the input photon except for the frequency (/ wavelength). Basically, it is a process by which a quantum state of light is shifted from its original frequency band to a desired one.

It has applications ranging from connecting disparate quantum systems (e.g., telecommunications-band quantum light sources with visible wavelength quantum memories to improved optical detection First-generation long-distance quantum repeater networks require quantum memories capable of interfacing with telecom

photons to perform quantum-interference-mediated entanglement generation operations. The ability to demonstrate these interconnections using real-life fibre connections in a long-distance setting is paramount to realize a scalable quantum internet.

6.2 Theory and Mathematical Model

A diamond configuration 4-level system is used for frequency conversion.

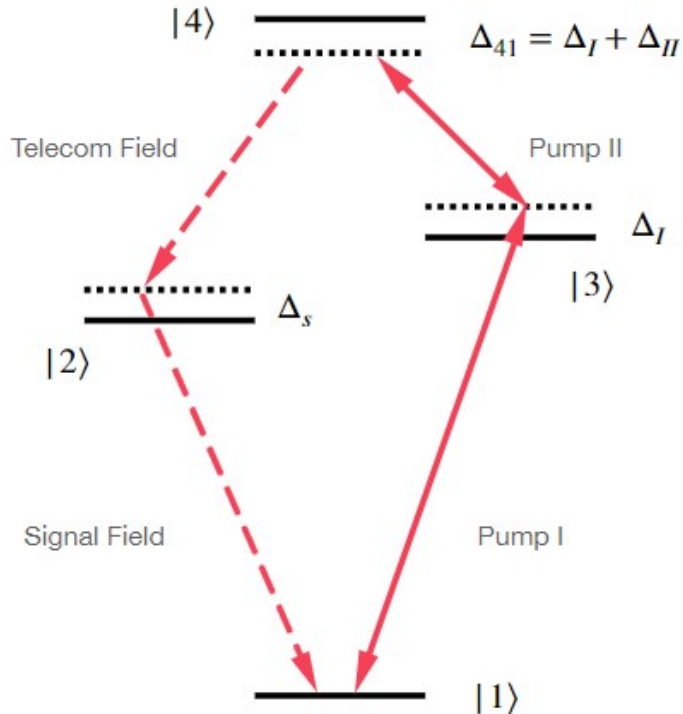


FIGURE 6.1: Diamond atomic scheme use for frequency conversion

The signal field (795nm) is the input which encodes the qubit information. The near resonance Pump I (780nm) and Pump II (1367nm) are strong CW pump fields. The telecom field (1324nm) is the generated field which encodes the same qubit information as that of the signal field. The Pump fields are given as

$$\vec{E}_I^{phy}(z, t) = \vec{E}_I(z)e^{-i(\omega_I t - \vec{k}_I \cdot \vec{z})} + c.c. \quad (6.1)$$

$$\vec{E}_{II}^{phy}(z, t) = \vec{E}_{II}(z)e^{-i(\omega_{II} t - \vec{k}_{II} \cdot \vec{z})} + c.c. \quad (6.2)$$

The model works on a reduced 4 level Hilbert space. Hamiltonian is

$$H = H_0 + V$$

H is the free Hamiltonian of the four system without the interaction with all the fields and has the form,

$$\hat{H}_0 = \begin{bmatrix} \hbar\omega_1 & 0 & 0 & 0 \\ 0 & \hbar\omega_2 & 0 & 0 \\ 0 & 0 & \hbar\omega_3 & 0 \\ 0 & 0 & 0 & \hbar\omega_4 \end{bmatrix} \quad (6.3)$$

rotating wave approximation is used to simplify the Hamiltonian. The Hamiltonian in rotating frame is

$$\tilde{H} = \hbar \begin{bmatrix} \omega_1 + \omega_{II} + \omega_I & -e^{i\phi}\Omega_s & -\Omega_I & 0 \\ -e^{-i\phi}\Omega_s & \omega_2 + \omega_t & 0 & -\Omega_t \\ -\Omega_I & 0 & \omega_3 + \omega_{II} & -\Omega_{II} \\ 0 & -\Omega_t & -\Omega_{II} & \omega_4 \end{bmatrix} \quad (6.4)$$

where

$$\Omega_I(z) \equiv \frac{\vec{E}_I(z) \cdot \vec{d}_{13}}{\hbar} \quad (6.5)$$

$$\Omega_{II}(z) \equiv \frac{\vec{E}_{II}(z) \cdot \vec{d}_{34}}{\hbar} \quad (6.6)$$

are the Laser Rabi frequencies, and

$$\begin{aligned} \Omega_s(z) &\equiv \frac{1}{\hbar} \left(\frac{\hbar\omega_s}{2V\epsilon_0} \right)^{\frac{1}{2}} \vec{e}_s \cdot \vec{d}_{12} \\ \Omega_t(z) &\equiv \frac{1}{\hbar} \left(\frac{\hbar\omega_t}{2V\epsilon_0} \right)^{\frac{1}{2}} \vec{e}_t \cdot \vec{d}_{24} \end{aligned} \quad (6.7)$$

are the single photon Rabi frequencies.

The evolution of the rotating frame density matrix is governed by the master equation

$$\dot{\tilde{\rho}} = -i[\tilde{H}, \tilde{\rho}] + \sum_{a>0} \left(L_a \tilde{\rho} L_a^\dagger - \frac{1}{2} L_a^\dagger L_a \tilde{\rho} - \frac{1}{2} \tilde{\rho} L_a^\dagger L_a \right) \quad (6.8)$$

The polarization of the medium is

$$P = n \text{Tr}(\rho d)$$

and the light propagation is governed by

$$\left(\nabla^2 - \frac{1}{c^2} \frac{\partial^2}{\partial t^2} \right) \vec{E} = \mu_0 \frac{\partial^2 \vec{P}}{\partial t^2} \quad (6.9)$$

Substituting the electric field equations of the signal and telecom and the polarization equation into the above light propagation equation, matching the terms with the same rotating frequency, we obtain the equations that couple the atomic states to the field envelopes.

$$\begin{aligned} \left(\frac{\partial}{\partial t} + c \frac{\partial}{\partial z} \right) \vec{\psi}_s(z, t) &= i \frac{\omega_s n V}{\epsilon_0} \tilde{\rho}_{21} \vec{d}_{12} \\ \left(\frac{\partial}{\partial t} + c \frac{\partial}{\partial z} \right) \vec{\psi}_t(z, t) &= i \frac{\omega_t n V}{\epsilon_0} \tilde{\rho}_{42} \vec{d}_{24} \end{aligned} \quad (6.10)$$

Together with the master equation, the three equations fully describe the conversion process. We conduct a numerical simulation to investigate the frequency response of the conversion process. The Mathematica runs the code for the master equation and gives us the matrix for computation. Now we solve to obtain the coherence densities

$$\begin{pmatrix} r2/r22 & r21 & -r12 & -r13 & -r14 \\ r21 & r22 & r22 & r23 & r24 \\ -r12 & r23 & r13 & r11 & r14 \\ -r13 & r11 & r13 & r34 & r13 \\ -r14 & r14 & r34 & r13 & r24 \end{pmatrix}$$

FIGURE 6.2: Density Matrix for 4-level transition

for the $|2\rangle$ to $|1\rangle$ transition and the $|4\rangle$ to $|2\rangle$ transition. We substitute these into the coupling equations and then solve the differential equation obtained. This would give us our final field envelope for the output signal field and the telecom field.

6.3 Simulation

In the simulation we apply several simplifications. We only consider an effective four-level system and ignore the effects from all hyper fine structures. We also completely ignore the Doppler effect from the motion of the atoms. We set the 780nm

and 1367nm pump to be CW light and the signal 795nm to be a Gaussian pulse. Since we ignore all the hyperfine levels, we do not expect an accurate conversion efficiency from the numerical simulation. Figure below shows a typical conversion process expected from the numerical simulation.

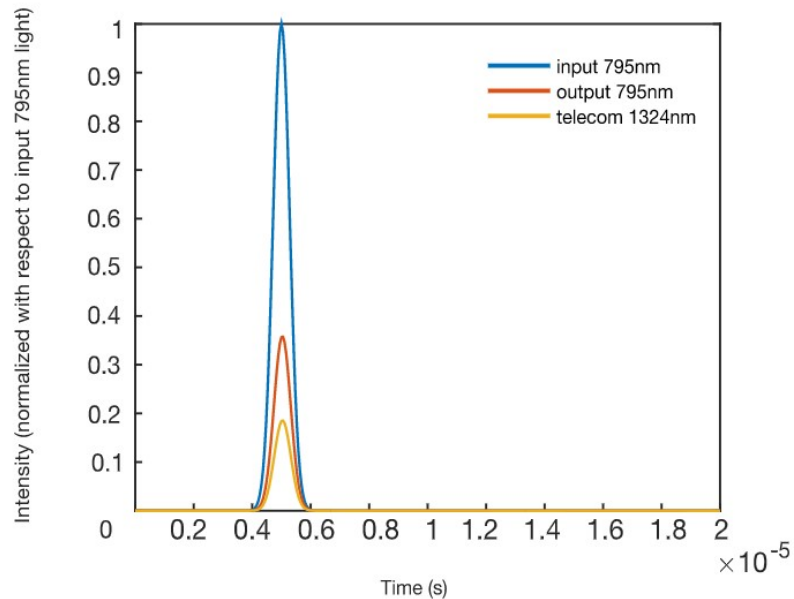


FIGURE 6.3: Intensity-Time curve obtained from the simulation of the frequency conversion process

Chapter 7

QFC

7.1 Laser Preparation

7.1.1 Laser Locking using CoSy

7.1.2 Laser Locking using Two-Photon Transition

7.2 Experimental Setup

Chapter 8

Integrating What We Have Covered

8.1 Integrated Setup of Polarization Encoded Qubits

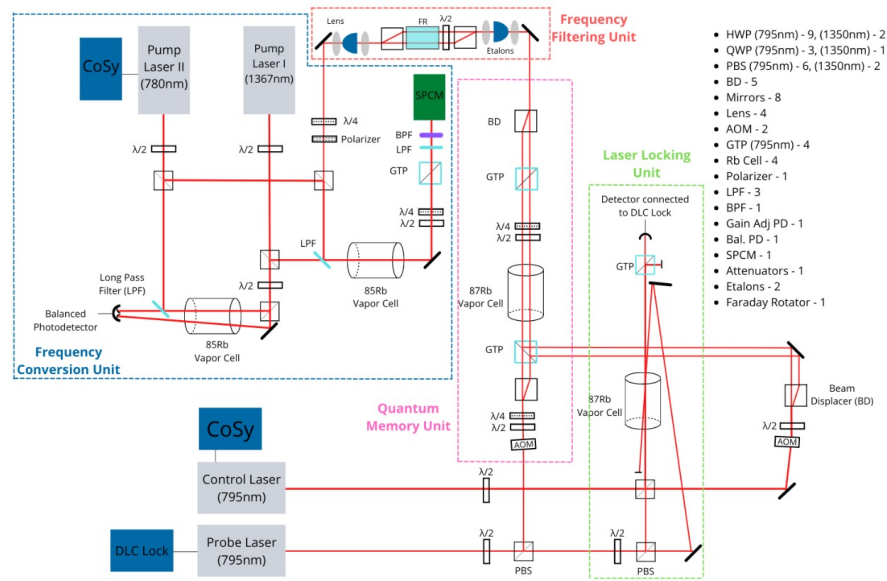


FIGURE 8.1: Experimental Setup Integrating QM, Frequency Filtering and QFC using Polarization Encoded Qubits

8.2 Integrated Setup of Time-bin Encoded Qubits

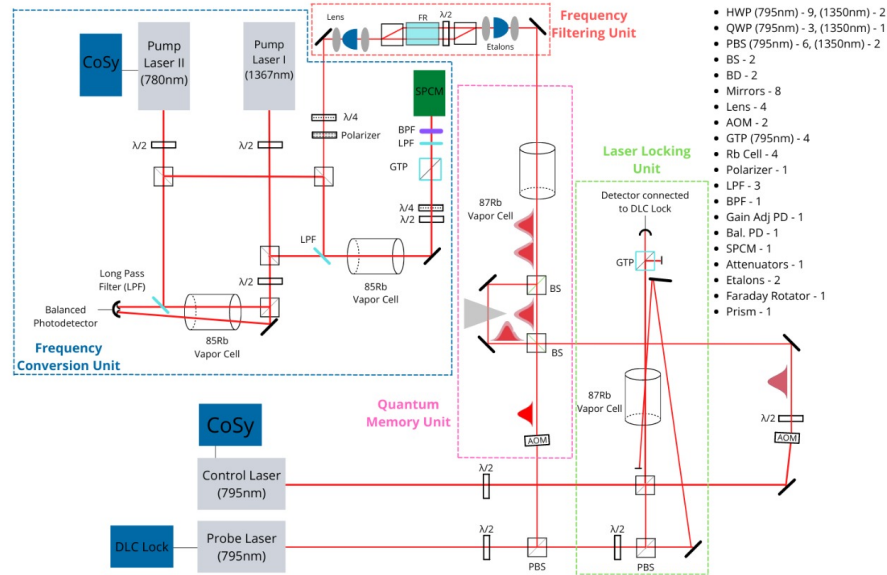


FIGURE 8.2: Experimental Setup Integrating QM, Frequency Filtering and QFC using Time Bin Encoded Qubits

Chapter 9

Miniaturisation of Concepts and Experiments

9.1 Gauss Chamber Design

9.1.1 Magnetic Shielding

The Gauss chamber is made of a Mu-metal which is used to shield the Rb vapor cell from the external magnetic fields produced by various components, primarily the Faraday Isolator, and even the Earth's magnetic field. Mu-metal is a soft magnetic alloy with exceptionally high magnetic permeability. The high permeability of mu-metal provides a low reluctance path for magnetic flux, leading to its use in magnetic shields against static or slowly varying magnetic fields. Magnetic shielding made with high-permeability alloys like mu-metal works not by blocking magnetic fields but by providing a path for the magnetic field lines around the shielded area.

But it saturates at a low magnetic field due to its low coercivity. Because mu-metal saturates at such low fields, sometimes the outer layer in such multilayer shields is made of ordinary steel. Its higher saturation value allows it to handle stronger magnetic fields, reducing them to a lower level that can be shielded effectively by the inner mu-metal layers. In order to create a magnetic field for the vapor cell, to observe, for eg, EIT in the presence of magnetic field (Zeeman Splitting) the innermost layer of the gauss chamber can be wrapped with a current carrying wire in order to make a solenoid.

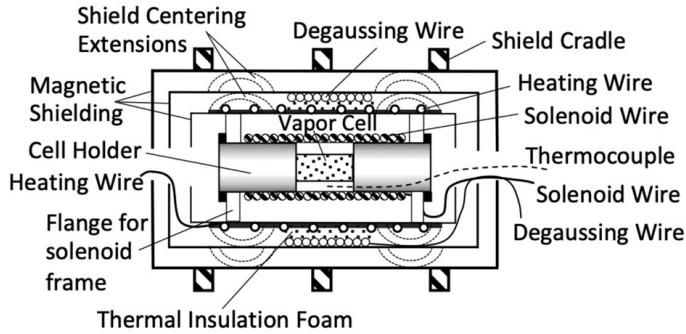


FIGURE 9.1: Full Diagram of Gauss Chamber

9.1.2 Heating Unit

The heater system to raise the alkali vapor temperature in order to increase the atomic density participating in EIT. This leads to an increase in the optical density which results in efficient storage without creating excessive amount of background noise. The Signal to Background ratio has to be measured in the 50°C - 65°C range to get the optimum temperature at which the Rb vapor cell should be maintained.

As seen in Fig. 9.1 [10], the vapor cell is kept in a cell holder, with a solenoid wire wrapped around the cell holder in order to produce a magnetic field (in order to observe the Zeeman effect). An electrically insulated non-magnetic heating wire is wound around the outer surface of the innermost mu-metal shield, for heating the entire volume of space enclosed by the innermost shield.

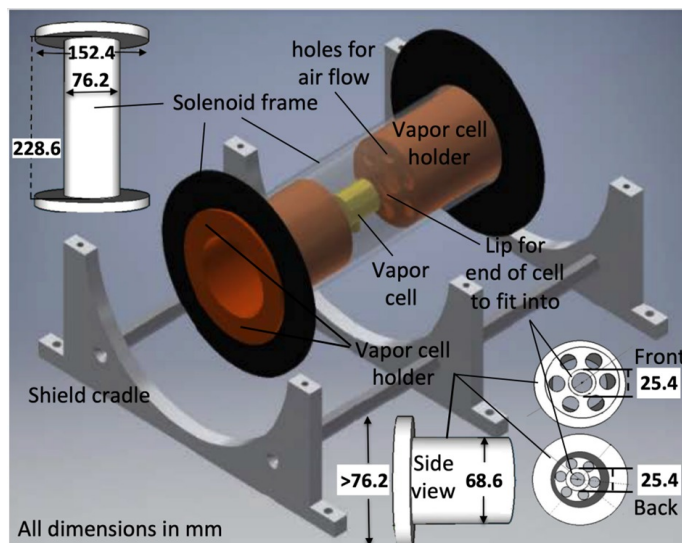


FIGURE 9.2: Inside view of Gauss Chamber

Above is a 3D view of the components inside the zero gauss chamber, with the

shields and solenoid wiring removed to display the vapor cell and holders. The holders are drawn slightly back to reveal the lip in which the ends of the vapor cell securely fit. The diameter of the black flanges for the solenoid frame are machined to be a close slide-fit inside the innermost mu-metal cylindrical shield. The top left inset shows the dimensions for the solenoid frame on which the wire is later wrapped. The three insets at the bottom right show the Front view of the vapor cell holder (i.e., axial view of holder as seen looking outward from center of chamber where vapor cell is located) depicting holes cut into each holder for air-flow, the Back view of cell holder (i.e., axial view as seen from outside chamber), and the Side view.

The vapor cell fits securely inside a lip provided on each holder, as shown in the figure above. A rubber O-ring is placed in the lip on each end of the cell to prevent the cell from jostling around. The holders are a close slide-fit inside the solenoid frame - the frame is shown in the top left inset. The vapor cell should be heated uniformly, so that “cold spots” not occur on the cell owing to thermal gradients. Holes are cut into the cell holders, as shown in the bottom right insets, to allow heated air to circulate, which significantly reduces the time needed for heating and increases the uniformity of the heating. To accurately control the cell temperature the heating wire current is controlled by reference to a thermistor placed near the cell.

9.2 Gauss Chamber Design

Several design factors affect the shielding factor of a Zero Gauss Chamber. For example:

- Increasing length to diameter ratio increases shielding factor
- Increasing mu-Metal thickness increases shielding factor
- Incorporating further layers into the MuChamber increases shielding factor

The typical L/D ratio is taken to be 1.65 which gives a shielding factor of 1210[38][39].

These factors must be taken care of in the miniaturization.

For the calculation of the reduction in the magnetic field by a single layer of the mu-metal by a simulation[33]:

B_{app} is the applied magnetic field just outside the single layer of the mu-metal. B_{in} is the magnetic field observed inside the mu-metal sheet (shaped like a cylinder). For the axial position: $B_{app} = 0.5$ T and $B_{in} = 0.077644$ T and $B_{in}/B_{app} = 0.155288$. For the transverse position: $B_{app} = 0.5$ T and $B_{in} = 0.00052795$ T and $B_{in}/B_{in} = 0.0010559$. This tells us that the main problem will be reducing the magnetic field along the axial position.

In the Faraday Isolator designed by Newport, “The external fields are designed to be well within federal safety guidelines which limit external fields from magnetic devices to be less than 2K Gauss at a radial distance of 5cm from the outside of the device”[28]. This wouldn’t create a problem in the tabletop experiment, as the Gauss Shielding and the distance between the frequency filtering setup will take care of the magnetic field reaching the Rb vapor cell. However, in the miniaturized version, shielding will not be that easy. If we design the components in a way where the QM module is in a separate box than the FF module, both could be covered with a combination of mu-metal sheets or sheets of iron/steel.

9.3 Filtering Unit

9.3.1 Temperature Controlled Etalons

9.3.2 Faraday Rotator

9.4 Quantum Memory Unit

9.4.1 Polarization Encoding

Since in polarization encoding, the encoding and decoding is done using wave plated and PBS respectively, miniaturisation of those components itself will do the trick.

9.4.2 Time Bin Encoding

Since time-bin encoding is done with the help of an MZI, which contains beam splitters, mirrors, and a prism, miniaturization of those components will do the trick. The SPCMs cannot be miniaturized.

Resolution of Time Bin Encoding

The encoding done for our time bin qubits depends on the resolution power of the SPCM, i.e. what is the minimum time difference between $|early\rangle$ and $|late\rangle$ bins such that the SPCM can resolve it. One might think that we would have to encode our qubits with a δt greater than the least count of the SPCM. But this is not the case. We can encode our qubits with a shorter δt and then increase the time difference between the bins.

This can be done by letting the bins pass through another MZI to increase the time difference between the two. This is done as follows:

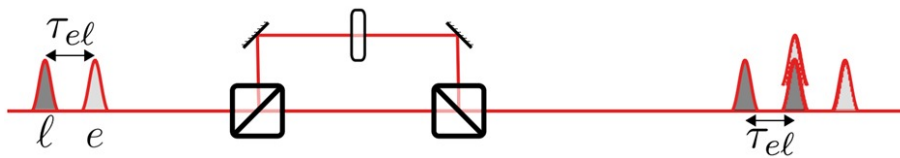


FIGURE 9.3: Increasing the time difference between $|early\rangle$ and $|late\rangle$

$\tau_{el} = \delta t$ The early and the late time bins are once again divided into further early and late time bins. The input time-bin state is sent through an unbalanced interferometer matched to the bin separation. Meaning whatever phase we used to create the time bins with the separation will be used again. The rightmost peak corresponds to $|early\rangle$ going through the short path again. The middle two peaks which are shown as overlapping correspond to $|early\rangle$ going through the longer path or the $|late\rangle$ going through the shorter path. The leftmost peak corresponds to $|late\rangle$ going through the long path.

The above will lead to an increase in the time separation between the early and the late bins. Isolating the middle pulse will be able to give us the correct measurement[11].

9.5 Quantum Frequency Conversion

9.5.1 Two-Photon Laser Locking Module

9.5.2 QFC Module

Chapter 10

Instruments and Vendors

10.1 Laser System

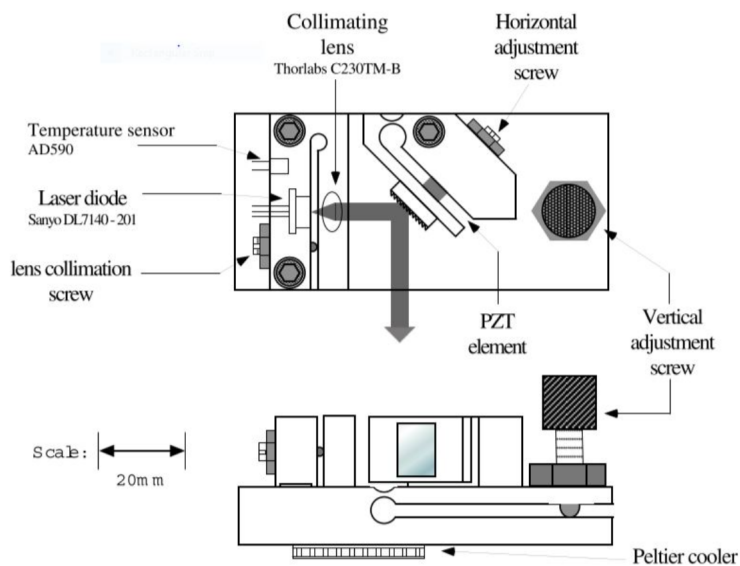


FIGURE 10.1: Schematic internal components of an ECDL Laser.
Source: [37]

We need a tunable, stable, and sufficiently narrow linewidth laser to work with a light-matter interaction system like ours. Hence, we use an external cavity diode laser, “Toptica DL Pro,” which can emit a laser beam from 765 nm to 805 nm. Our laser module is optimized for 780 nm for interacting with the D2 line of Rubidium transitions. The construction of an ECDL laser is shown in the diagram below. The diode emitting laser is coupled to a grating whose position can be controlled by a piezo. The voltage across the piezo is thus used to control the frequency of the output laser beam. Apart from the DC voltage, other parameters like current, temperature, and voltage offset are essential for precisely controlling the laser output

frequency. Hence, these parameters are carefully controlled. The laser frequency is swept around an atomic transition of the Rb atom, or it is locked at a particular frequency using a PID controlled loop. The PID loop is implemented with the DLC Pro Locking module, which takes input from the detection of the laser after interacting with the Rb atoms, and locks the laser at the top of the fringe or any other setting.

10.2 Wavelength Meter

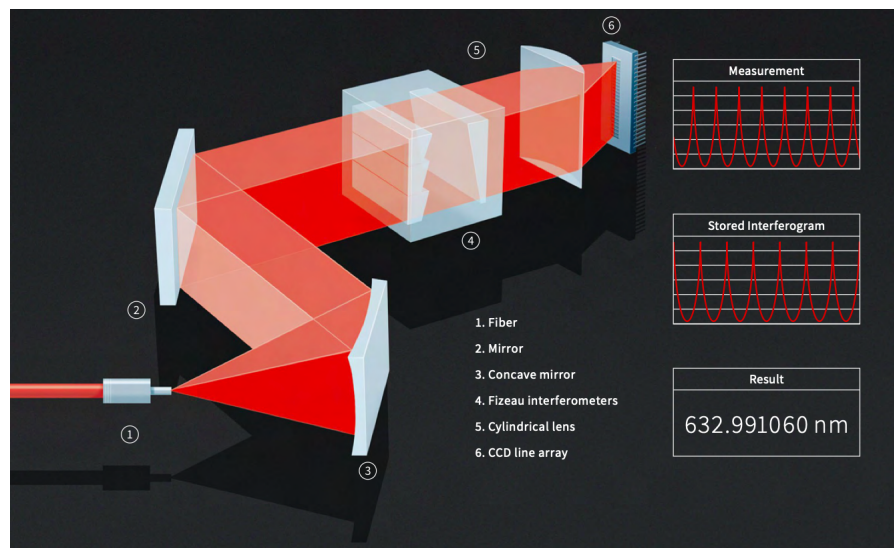


FIGURE 10.2: Schematic of a Wavelength Meter. Source: HighFinesse Datasheet.

We used HighFinesse wavelength meter to measure the wavelength of the lasers in the lab. The laser output is coupled to the wavelength meter (WM) via an optical fiber cable. The beam is expanded inside the WM and falls onto a concave mirror, making the beam parallel to the propagating axis. The beam then reflects from a mirror and passes through a Fizeau interferometer. The beam coming out of the interferometer is passed through a cylindrical lens onto an array of charge-coupled detector arrays. The interference pattern recorded from the detection is compared to the previously stored calibrating data pattern. After comparison, the software outputs the wavelength up to kHz precision.

10.3 Beam Master for Beam profile measurement

We have Coherent Beam Master in our lab, which is a beam profiler based on multiple knife-edge scanning techniques. The knife edges are placed on a rotating drum, giving scans from different axes in a single rotation. The scans are then combined tomographically to reconstruct the profile of the beam. Beam Master gives the input

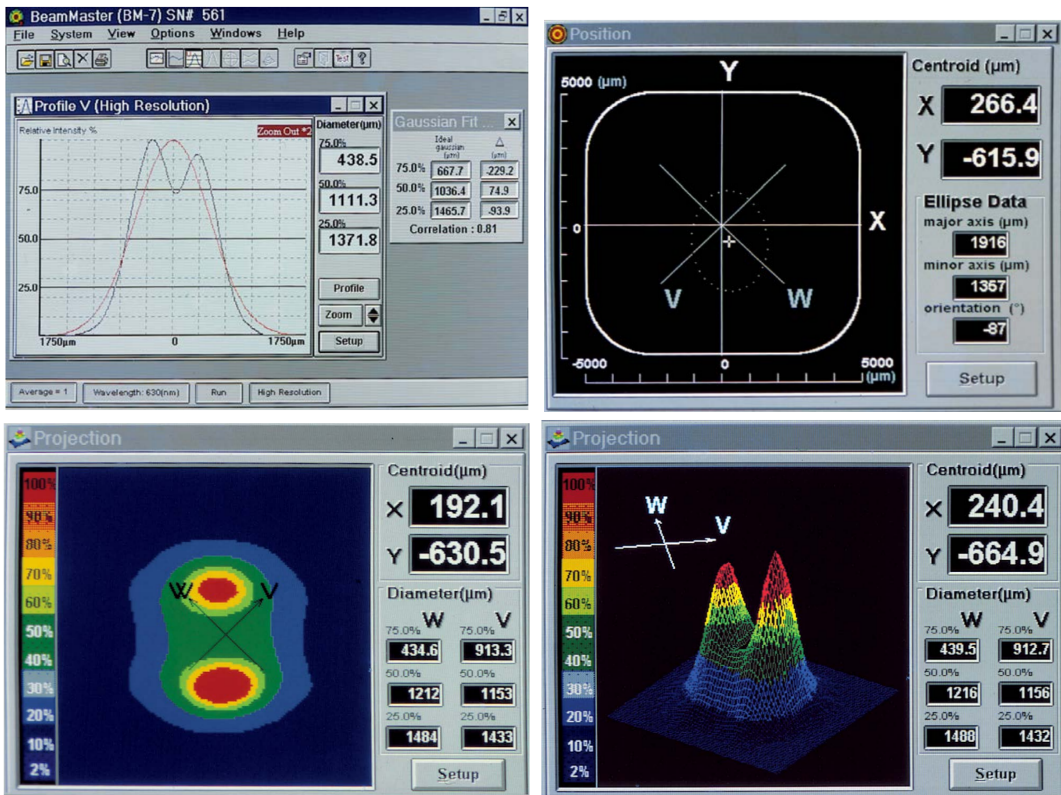


FIGURE 10.3: Software interface of Coherent Beam Master. It measures the beam diameter along V and W axis. It also gives the heatmap of the intensity of the laser beam. Source: Coherent Beam Master Datasheet.

laser beam profile (Gaussian nature), position and ellipticity, width, power, and 3D intensity plots. Its USB interface helps in-situ calibrate the beam profile, width, ellipticity, and other beam parameters. Shown are some of the measurements done in the lab (Refer to Fig. 3.2 and Fig. 3.1.)

10.4 Power Meter

A power meter is essential for the experiments. It is frequently used to measure the power of the laser beam in experiments. Other theoretical parameters like Rabi

frequency, intensity, etc., are calculated from the data observed from a power meter and a beam profiler.



FIGURE 10.4: Powermeter with a sensing unit and a screen to display the power falling on it upto 100 nW level. Source: CNI Optics Inc.

10.5 Acousto Optic Modulator

An AOM consists of a quartz crystal attached to a piezoelectric transducer. The transducer is connected to a radio frequency driver, producing sound waves of frequency from 78 MHz to 133 MHz. The piezo produces a sound wave inside the crystal, which produces expansion and contraction. The expansion and contraction lead to a variation in the crystal's refraction index. When an optical field falls on the crystal, it suffers Bragg-like diffraction due to the refractive index grating. Therefore the field is diffracted either in the +1 or -1 order depending on the angle of incidence of the optical field. The 0th-order beam passes through the crystal without any deviation, while the higher-order beams reflect from the planes of the index grating. The +1 (-1) order shifts the optical field frequency to $\nu + \nu_{RF}(\nu - \nu_{RF})$, where ν_{RF} is the frequency of the RF driver. An AOM may work as a beam deflector, frequency shifter, or optical switch. Since the AOM deviates the beam by an angle $2\theta_B$, it can be used as a beam deflector. It can either add to or deduct the RF frequency from the optical frequency, acting as a frequency shifter. The AOM works like an optical switch in the higher-order deflected beams if the RF source is modulated to produce

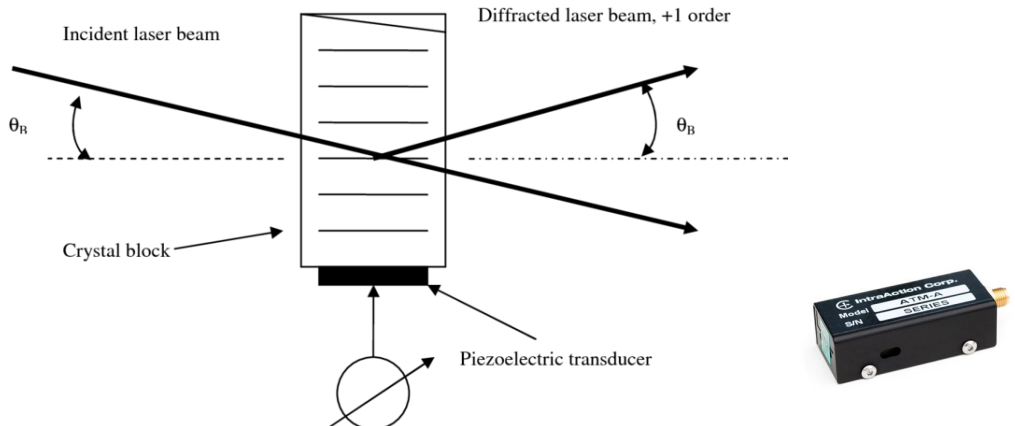


FIGURE 10.5: Schematic of an AOM aligned in the +1 order. An AOM from IntraAction is shown on the right. Source: IntraAction.

pulsed signals. We have used AOM-110 and RF drivers from IntraAction in our experiments.

10.6 Oscilloscope and Pulse generator

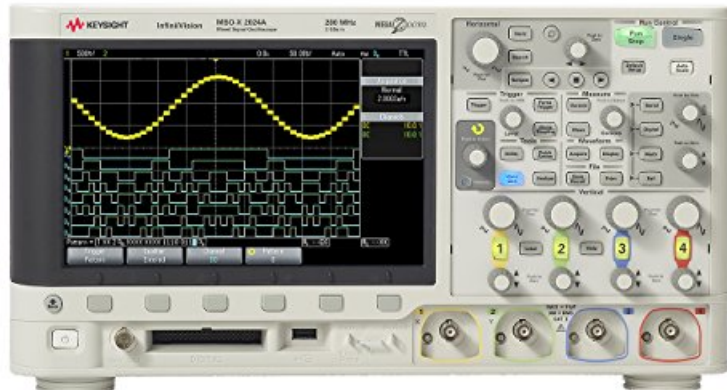


FIGURE 10.6: Oscilloscope from Keysight Technologies used for generating pulses and displaying signals. Source: Keysight Technologies.

We used an oscilloscope from Agilent Technologies (now Keysight Technologies) model id MSO X-4054A. The oscilloscope supports a high bandwidth (500MHz) with a high sampling rate (5 GSa/s). We can view up to 4 signals from different channels on the same screen with color coding. This helps in viewing signals from detectors, FPI, and pulse generators simultaneously on the same screen. The detection of

FPI and detector signals helps calibrate the signal detuning (discussed in the experiments section).

The oscilloscope has a built-in pulse/frequency generator with precise amplitude, phase, frequency, and offset control. We use this feature extensively in our experiments. We can choose from several patterns of frequency generation, e.g., sine wave, triangular wave, square wave, arbitrary waveform, and so on. Waveforms generated are presented in later sections.

10.7 Photo Detectors



FIGURE 10.7: Silicon gain adjustable photodetector from Thorlabs Inc. Source: Thorlabs.

We use photodetectors from Thorlabs product id PDA-36A. The photodetector is a switchable gain, silicon-based detector. The adjustable gain feature is useful when working with very low power signals.

10.8 Rubidium Vapor Cell

We use Rubidium vapor cells from Thorlabs. It comes in a borosilicate cell to protect from chipping and cracking. It contains Rubidium in natural isotope ratio, which is 72.15% ^{85}Rb and 27.85% ^{87}Rb .



FIGURE 10.8: Borosilicate Rb vapor cell from Thorlabs Inc. Source: Thorlabs.

10.9 Gauss Chamber



FIGURE 10.9: A typical design of a Gauss Chamber. It has three-layers of μ -metal shielding in a cylindrical box with holes of size of the diameter of the Rb vapor cell on the end-caps.

It contains 3-layers of mu-metal for magnetic field shielding. The vapor cell is placed at the chamber's center in a glass-fit socket. Holes on the lids allow access to laser beams to interact with the atomic vapor inside the chamber.

10.10 Fabry-Perot Interferometer

We use FPI-100 from Toptica Photonics as a frequency scale in our system. The FPI consists of a set of parallel mirrors with a built-in photodetector. We use a miniScan102 generator to scan the FPI. The FSR of this FPI is 1 GHz, and it can be used in

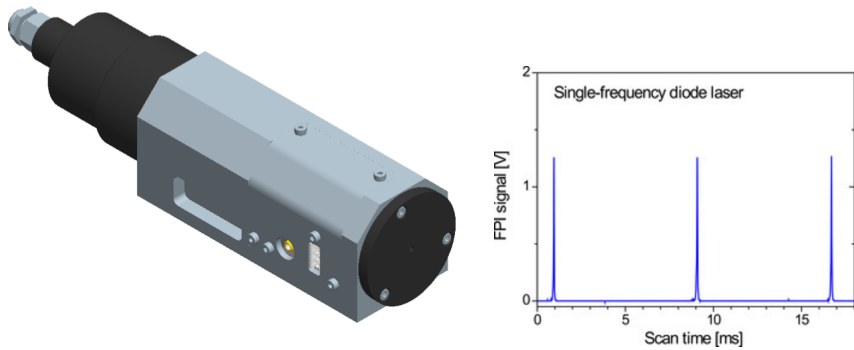


FIGURE 10.10: Fabry-Perot interferometer used in our lab with its typical spectrum beside it. The separation of the peaks is a characteristic of the FPI. We use an FPI with $FSR = 1\text{GHz}$. Source: Toptica Photonics.

the wavelength range of our system i.e., around 800 nm. A typical FPI spectrum is shown in the figure below. The peak-to-peak separation in the spectrum is equivalent to 1 GHz of frequency.

Bibliography

- [1] Shamiul Alam, Md Shafayat Hossain, and Ahmedullah Aziz. "A non-volatile cryogenic random-access memory based on the quantum anomalous Hall effect". In: *Scientific reports* 11.1 (2021), pp. 1–9.
- [2] Karol Bartkiewicz, Antonín Černoch, and Karel Lemr. "Using quantum routers to implement quantum message authentication and Bell-state manipulation". In: *Physical Review A* 90.2 (2014), p. 022335.
- [3] Peter Beyersdorf. *Mode Matching for Etalons*. URL: <https://www.youtube.com/watch?v=5bR6wkZGa18>.
- [4] K-J Boller, A Imamoğlu, and Stephen E Harris. "Observation of electromagnetically induced transparency". In: *Physical Review Letters* 66.20 (1991), p. 2593.
- [5] Jonatan Bohr Brask, Rafael Chaves, and Jan Kołodyński. "Improved quantum magnetometry beyond the standard quantum limit". In: *Physical Review X* 5.3 (2015), p. 031010.
- [6] J. Brendel et al. "Pulsed Energy-Time Entangled Twin-Photon Source for Quantum Communication". In: *Phys. Rev. Lett.* 82 (12 1999), pp. 2594–2597. DOI: [10.1103/PhysRevLett.82.2594](https://doi.org/10.1103/PhysRevLett.82.2594). URL: <https://link.aps.org/doi/10.1103/PhysRevLett.82.2594>.
- [7] H-J Briegel et al. "Quantum repeaters: the role of imperfect local operations in quantum communication". In: *Physical Review Letters* 81.26 (1998), p. 5932.
- [8] Félix Bussières et al. "Prospective applications of optical quantum memories". In: *Journal of Modern Optics* 60.18 (2013), pp. 1519–1537.
- [9] John Chiaverini et al. "Realization of quantum error correction". In: *Nature* 432.7017 (2004), pp. 602–605.

- [10] Kenneth DeRose et al. *Producing slow light in warm alkali vapor using electromagnetically induced transparency*. 2020. DOI: [10.48550/ARXIV.2011.09229](https://doi.org/10.48550/ARXIV.2011.09229). URL: <https://arxiv.org/abs/2011.09229>.
- [11] John M. Donohue et al. “Coherent ultrafast measurement of time-bin encoded photons”. In: *Physical Review Letters* 111.15 (2013). DOI: [10.1103/physrevlett.111.153602](https://doi.org/10.1103/physrevlett.111.153602).
- [12] Artur Ekert and Chiara Macchiavello. “Quantum error correction for communication”. In: *Physical Review Letters* 77.12 (1996), p. 2585.
- [13] Boston Electronics. *Single Photon Counting Detectors for TCSPC*. URL: https://www.boselec.com/wp-content/uploads/PhotonCounting/Becker&Hickl/bhLiterature/B_H_Photon_Counting_Detectors_5-16-2016.pdf.
- [14] Delta Optical Thin Film. *Bandpass Filters*. URL: <https://tinyurl.com/jpp6528f>.
- [15] Michael Fleischhauer, Atac Imamoglu, and Jonathan P Marangos. “Electromagnetically induced transparency: Optics in coherent media”. In: *Reviews of modern physics* 77.2 (2005), p. 633.
- [16] Vittorio Giovannetti, Seth Lloyd, and Lorenzo Maccone. “Advances in quantum metrology”. In: *Nature photonics* 5.4 (2011), p. 222.
- [17] Vittorio Giovannetti, Seth Lloyd, and Lorenzo Maccone. “Quantum metrology”. In: *Physical review letters* 96.1 (2006), p. 010401.
- [18] Alexey V Gorshkov et al. “Universal approach to optimal photon storage in atomic media”. In: *Physical review letters* 98.12 (2007), p. 123601.
- [19] Stephen E Harris, JE Field, and A Imamoğlu. “Nonlinear optical processes using electromagnetically induced transparency”. In: *Physical Review Letters* 64.10 (1990), p. 1107.
- [20] Khabat Heshami et al. “Quantum memories: emerging applications and recent advances”. In: *Journal of modern optics* 63.20 (2016), pp. 2005–2028.
- [21] Sebastian P. Horvath et al. “Noise-free on-demand atomic frequency comb quantum memory”. In: *Phys. Rev. Research* 3 (2 2021), p. 023099. DOI: [10.1103/PhysRevResearch.3.023099](https://doi.org/10.1103/PhysRevResearch.3.023099). URL: <https://link.aps.org/doi/10.1103/PhysRevResearch.3.023099>.

- [22] Mahdi Hosseini et al. "High efficiency coherent optical memory with warm rubidium vapour". In: *Nature communications* 2.1 (2011), pp. 1–5.
- [23] University of Arizona Joshua Brent. *Dual Etalon Tunable Filter with Feedback Control*. URL: <https://www.optics.arizona.edu/sites/optics.arizona.edu/files/joshua-brent-report.pdf>.
- [24] H Jeff Kimble. "The quantum internet". In: *Nature* 453.7198 (2008), pp. 1023–1030.
- [25] Chao Liu et al. "On-Demand Quantum Storage of Photonic Qubits in an On-Chip Waveguide". In: *Phys. Rev. Lett.* 125 (26 2020), p. 260504. DOI: [10.1103/PhysRevLett.125.260504](https://doi.org/10.1103/PhysRevLett.125.260504). URL: <https://link.aps.org/doi/10.1103/PhysRevLett.125.260504>.
- [26] Alexander I Lvovsky, Barry C Sanders, and Wolfgang Tittel. "Optical quantum memory". In: *Nature photonics* 3.12 (2009), pp. 706–714.
- [27] Mehdi Namazi. "A Scalable Room-Temperature Quantum Processing Network". In: *Ph. D. Thesis* (2018).
- [28] Newport. *Newport Faraday Rotator*. 2005. URL: https://www.newport.com/medias/sys_master/images/images/haa/h84/8797197271070/LP-ISO-User-Manual.pdf.
- [29] LLC Omega Optical. *Longpass and Shortpass Filters*. URL: <https://www.omegafilters.com/product-types/longpass-shortpass>.
- [30] Jian-Wei Pan et al. "Multiphoton entanglement and interferometry". In: *Reviews of Modern Physics* 84.2 (2012), p. 777.
- [31] Nathaniel B. Phillips. "Slow and stored light under conditions of electromagnetically induced transparency and four wave mixing in an atomic vapor". Copyright - Database copyright ProQuest LLC; ProQuest does not claim copyright in the individual underlying works; Last updated - 2021-05-14. PhD thesis. 2011, p. 192. URL: <https://www.proquest.com/dissertations-theses/slow-stored-light-under-conditions/docview/916791204/se-2?accountid=27544>.

- [32] Daryl W Preston. "Doppler-free saturated absorption: Laser spectroscopy". In: *American Journal of Physics* 64.11 (1996), pp. 1432–1436.
- [33] QuickField. *Calculation of the reduction in the magnetic field by a single layer of mu metal by a simulation*. URL: https://quickfield.com/advanced/mu-metal_shielding.htm.
- [34] KF Reim et al. "Towards high-speed optical quantum memories". In: *Nature Photonics* 4.4 (2010), pp. 218–221.
- [35] Valerio Scarani et al. "The security of practical quantum key distribution". In: *Reviews of modern physics* 81.3 (2009), p. 1301.
- [36] Christoph Simon et al. "Quantum memories". In: *The European Physical Journal D* 58.1 (2010), pp. 1–22.
- [37] Siddhant Singh. "EIT with and without Magnetic Field". In: (2020).
- [38] Magnetic Shields Co UK. *Zero Gauss Chamber by Magnetic Shields Co UK*. URL: https://magneticshields.co.uk/multisites/mumetalfoil/index.php?option=com_content&view=article&id=3&Itemid=3.
- [39] Magnetic Shields Corporation USA. *Important Brochure for Gauss Chamber*. URL: <http://www.leadingedgemetals.com/pdfs/ZG-3-Zero-Gauss-Chambers-Brochure.pdf>.